Application of the Aerostrip for Aerodynamic Optimisation in Motorsport

EM401 Final Report

Student: Max Stancliffe

Registration: 202128722

Signature: Date: 04 April 2025

Supervisor: Gordon Dobie

Abstract

The application of Pressure Profile Systems' (PPS) Aerostrip as an aerodynamic testing tool in a motorsport context is explored. The Aerostrip, a flexible and reusable sensor capable of measuring surface pressure distributions in real time, is implemented onto a Formula 1-style rear wing and tested in a controlled wind tunnel environment. Pressure data from both the upper and lower surfaces is used to calculate pressure differentials and estimate downforce. Tests are conducted at freestream velocities of 10 m/s and 15 m/s, producing experimental downforce values of 48.56 N and 95.07 N, respectively.

Two sensor configurations were tested: 20 mm pitch elements for large-scale pressure trends and 8 mm pitch for fine-resolution data near the leading edge of the wing element. These configurations produced consistent pressure profiles and evidence of mid-chord flow separation was observed. A minor pressure variation across the wingspan was measured, with the lower surface showing a 13.4% variation, highlighting the influence of manufacturing tolerances, mounting imperfections and other real-world effects often neglected in simulations.

To compare and validate experimental findings, an identical model of the wing and custom bracket system is recreated for Computational Fluid Dynamics (CFD) simulations using Siemens STAR-CCM+. Multiple turbulence models, k-ω SST, k-ε and Spalart-Allmaras, were tested and compared against measured data to identify the most accurate predictive model. The k-ω SST model showed the closest agreement, particularly in regions with steep pressure gradients, predicting downforce values of 53.87 N at 10 m/s and 124.89 N at 15 m/s. These values overpredicted downforce by 10.9% and 31.4%, respectively. Variations may result from limitations in RANS turbulence modelling, particularly in predicting real-world aerodynamic effects such as boundary layer separation and viscous losses.

The Aerostrip proved to be an effective and efficient tool for analysing aerodynamic forces, measuring pressure distribution and validating CFD outputs. Its high resolution, ease of use and compatibility with modern simulation workflows make it a promising alternative to traditional testing methods in motorsport, particularly under strict resource constraints where flexible and efficient solutions are needed.

Contents

List of Figures

Nomenclature

Abbreviation	Description
PPS	Pressure Profile Systems
USM	University of Strathclyde Motorsport
CFD	Computational Fluid Dynamics
PIV	Particle Image Velocimetry
PSP	Pressure-sensitive Paint
FIA	Fédération Internationale de l'Automobile
E1	Element 1

1 Introduction

Aerodynamic efficiency plays a critical role in motorsport, where even marginal improvements in airflow management can significantly enhance vehicle performance. This study examines the practical application of Pressure Profile Systems' (PPS) Aerostrip as a surface pressure measurement tool to support real-world aerodynamic testing in a motorsport environment. The Aerostrip is a flexible sensor strip designed to collect surface pressure data at discrete points along an array to analyse airflow behaviour. While previous studies have already validated the sensor's accuracy, this study assumes the technology's reliability and shifts the focus toward its application in high-performance race car development.

Tests are performed on a multi-element, Formula 1-style rear wing provided by the University of Strathclyde Motorsport (USM) team. The wing is tested under controlled wind tunnel conditions, with Aerostrip sensor strips mounted on the upper and lower surfaces of the main element. The measured data enables a detailed analysis of pressure differentials and downforce, providing insight into real-world aerodynamic factors such as boundary layer flow separation, viscous effects and turbulent wake structures.

Alongside experimental testing, Computational Fluid Dynamics (CFD) simulations are conducted using Siemens STAR-CCM+ to compare results with physical measurements. These simulations enable the analysis of curve shapes, trends and discrepancies to improve the accuracy of future aerodynamic models. By comparing sensor-derived pressure data with CFD results, differing turbulence models can be analysed to verify the suitability and validity of the simulation setup.

Two Aerostrip configurations with different sensor resolutions are tested: sensor strips with elements of 20 mm pitch are utilised to observe large-scale aerodynamic trends, while a finer 8 mm pitch element configuration enables a detailed investigation of pressure peaks and measurement accuracy. Pressure data is collected using PPS's Chameleon software, which provides real-time monitoring, data processing and visualisation to allow for precise interpretation of the pressure distribution and supporting airflow optimisation during setup.

As a new aerodynamic testing method, the Aerostrip offers unique advantages, including flexibility and reusability, while introducing new challenges compared to traditional aerodynamic testing methods, such as pressure taps or pressure-sensitive paint. This study evaluates Aerostrip's practical applicability, usability and limitations while aiming to demonstrate its potential for streamlining aerodynamic testing processes, supporting simulation validation and enabling more sustainable and accessible aerodynamic development in motorsport.

2 Literature Review

2.1 Development of the Aerostrip

The Aerostrip, designed for non-intrusive, high-resolution surface pressure measurements, has been validated in experimental studies, demonstrating its accuracy, repeatability and suitability for both controlled laboratory testing and real-world environments.

Zhang et al. [1] conducted a study on the application of Aerostrip sensors in automotive aerodynamics, testing on a passenger car under both controlled wind tunnel conditions and real-world road tests. The sensors were shown to produce highly accurate pressure measurements while maintaining minimal interference with the flow. Particle Image Velocimetry (PIV) revealed that the sensor's influence on the surrounding airflow is below 4%, confirming that the 1.44mm thick sensor strip does not significantly disturb local aerodynamics. The study also compared sensor readings against CFD simulations, showing a strong agreement in pressure trends and spatial distributions. Experimental results highlight Aerostrip's capability in real-time aerodynamic testing without the need for invasive installations such as pressure taps.

Subramanian et al. [2] further validated Aerostrip's performance through controlled laboratory tests across various aerodynamic conditions, providing a detailed evaluation of the sensor's capabilities in simple and complex aerodynamic scenarios. The study first validated the sensor's reliability and stability under static conditions by comparing pressure readings inside a plenum chamber against a high-precision reference sensor. The results showed excellent agreement with minimal pressure variations, confirming the sensor strip's reliability in precise testing environments. The Aerostrip was also tested against external flow conditions on a circular cylinder inside a wind tunnel to analyse pressure distributions across various flow regions. The measured values closely align with recorded data from a Scanivalve pressure scanner, demonstrating the sensor's effectiveness in capturing surface pressure data in aerodynamic flows.

Additionally, a PIV investigation was conducted to assess how the Aerostrip affects boundary layer development when mounted on a flat surface. Results showed that while small velocity fluctuations were observed near individual sensing elements, the overall flow disturbance remained minimal, with no significant separation detected. This reinforces the conclusion that the Aerostrip can be installed on sensitive aerodynamic surfaces without introducing flow distortion.

These studies establish that Aerostrip provides reliable and accurate pressure data, providing a strong foundation to shift to more specialised aerodynamic environments, such as motorsport testing.

Building on this validation, the current study extends Aerostrip's application for analysing pressure differentials on a Formula 1-style rear wing under wind tunnel conditions. The project aims not only to demonstrate the Aerostrip's effectiveness as

a measurement tool but also as a strategic resource for aerodynamic development and model validation in high-performance racing environments.

2.2   Traditional Aerodynamic Testing Methods

Aerodynamic testing is crucial for optimising vehicle stability, downforce and efficiency. Advanced techniques such as Particle Image Velocimetry (PIV) provide detailed and accurate descriptions of airflow patterns around a race car. PIV is a flow visualisation method that measures fluid velocity by tracking the motion of illuminated tracer particles in successive images. Martins et al. [3] investigated the aerodynamic interaction between a Formula 1-style front wing and a wheel in ground effect, examining how variations in wing pressure distribution influence downstream wake characteristics. Their findings highlight the significant role of a wing's aerodynamic properties in wake development and demonstrate how pressure distribution affects overall aerodynamic performance. While PIV captures transient flow structures with high resolution, it requires significant computational resources to be successful.

Another technique for measuring pressure to analyse airflow behaviour involves the use of small holes drilled into a surface, known as pressure taps. These taps measure static pressure at discrete points through long plastic tubes connected to a pressure transducer, with strain gauges detecting pressure at each surface tap. While this method is precise, it is both invasive and structurally damaging to test models. Li et al. [4] conducted wind tunnel experiments on high-speed train aerodynamics, utilising pressure taps to monitor pressure distributions across different yaw angles. The investigation demonstrated that pressure taps effectively capture localised aerodynamic effects while also highlighting the method's sensitivity to symmetry discrepancies and boundary layer variations. The Aerostrip works similarly to pressure taps, collecting surface pressure measurements, but offers a non-invasive and flexible alternative.

Pressure-sensitive Paint (PSP) is a fluid-based coating applied to a test surface to measure local pressure distributions in aerodynamic testing. The luminescent molecules in the paint, when exposed to ultraviolet (UV) light, emit fluorescence with a varying intensity according to local air pressure [5]. This technique enables high-resolution surface pressure mapping without the need for intrusive physical taps or transducers. Aider et al. [6] investigated the application of PSP in automotive aerodynamics by comparing experimental results with those from conventional pressure taps and CFD simulations on a 1/4-scale Peugeot 206 wind tunnel model. The study demonstrated a quantitative agreement between PSP and pressure tap measurements, with PSP offering a superior spatial resolution as it recorded finer pressure variations across the vehicle surface. However, while this technique eliminates the need for drilling pressure taps, it requires a controlled environment with stable lighting conditions and careful calibration to mitigate temperature sensitivity. Additionally, PSP is a permanent coating, meaning test models remain covered in paint after application, which may limit reuse or require additional surface preparation for

future tests. Despite these challenges, PSP remains a valuable alternative to standard pressure measurement techniques.

2.3 Sensor Overview & Application

The Aerostrip consists of 12 micro-scale pressure sensors embedded on a 0.1 mm flexible PCB, allowing for the analysis of curved surfaces. Each sensor element uses piezoresistive absolute pressure measurement, with factory calibration and embedded temperature compensation ensuring accuracy across different test conditions [1]. The pressure data is collected and transmits real-time data to a USB-powered U400 DAQ microcontroller, streaming at a maximum rate of 200 Hz [2].

2.3.1 Sensor Pitch Calculation

The sensor pitch (p) defines the spacing between individual pressure sensors along the strip. This is determined by:

$$p = \frac{L_{max} - L_{electronics}}{n} \tag{1}$$

Where:

- L_{max} is the maximum length of the sensor strip (mm)
- $L_{electronics}$ is the reserved space for electronics (mm)
- n is the number of sensing elements (e.g. 12)

This study utilises 20 mm pitch sensing elements along an array to analyse large-scale aerodynamic trends.

To accommodate higher spatial resolution for detecting fine-scale aerodynamic features such as pressure recovery, an 8mm pitch configuration is also used, increasing the number of sensors per unit length.

2.3.2 Comparison of Sensor Pitches
- 20 mm pitch: Coarser resolution, suitable for identifying large-scale aerodynamic trends, and reduces data processing time.
- 8mm pitch: Finer resolution, ideal for capturing pressure peaks and boundary layer development, but requires extended data processing.

2.4 Pressure Differentials in Aerodynamics

Aerodynamics play a fundamental role in race car performance, particularly in high-speed motorsport such as Formula 1. The rear wing is a critical aerodynamic component that influences airflow to generate downforce, improving traction, cornering speed and braking stability [7]. This effect is achieved by creating a pressure differential between the upper and lower wing surfaces, where a high-pressure zone forms on the upper surface and a low-pressure zone develops beneath it. The resulting downward force (downforce) enhances grip on the track and stabilises vehicle dynamics. A visual representation of this pressure differential is given in Figure 1.

High-Pressure
Slower Air

Low-Pressure
Faster Air
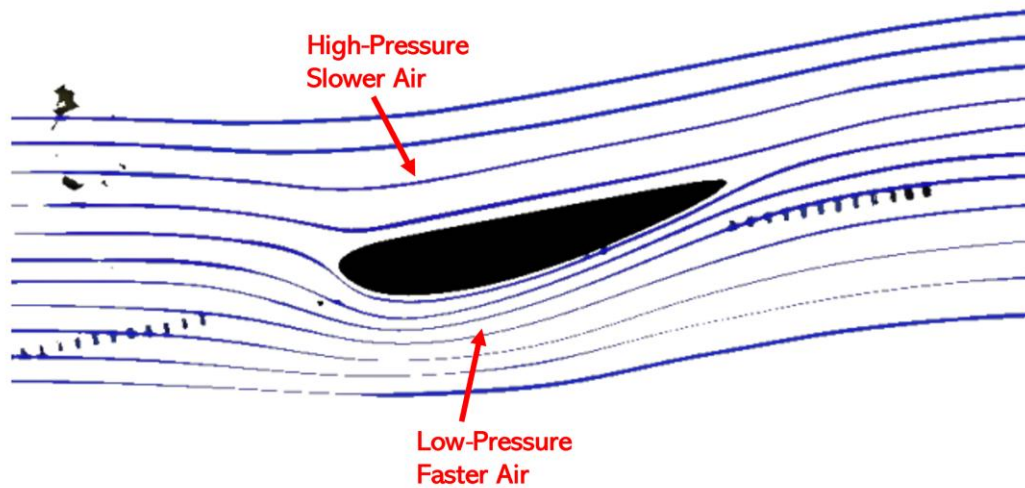
Figure 1 – Wing shape illustrating airflow over the surface and how varying wind velocity affects pressure on the upper and lower surfaces. Adapted from [8].

However, while increased downforce improves handling, it also leads to higher aerodynamic drag, which resists forward motion and reduces top speed, particularly on straight sections of a circuit. Drag is mainly caused by airflow separation and turbulence, optimising the downforce-to-drag balance is a crucial aspect of motorsport aerodynamics. The design and placement of a rear wing significantly influences this balance, requiring careful aerodynamic tuning. Qiu et al. [9] investigated various rear-wing designs and setups to demonstrate how different configurations can be optimised to enhance racing conditions and overall automotive performance.
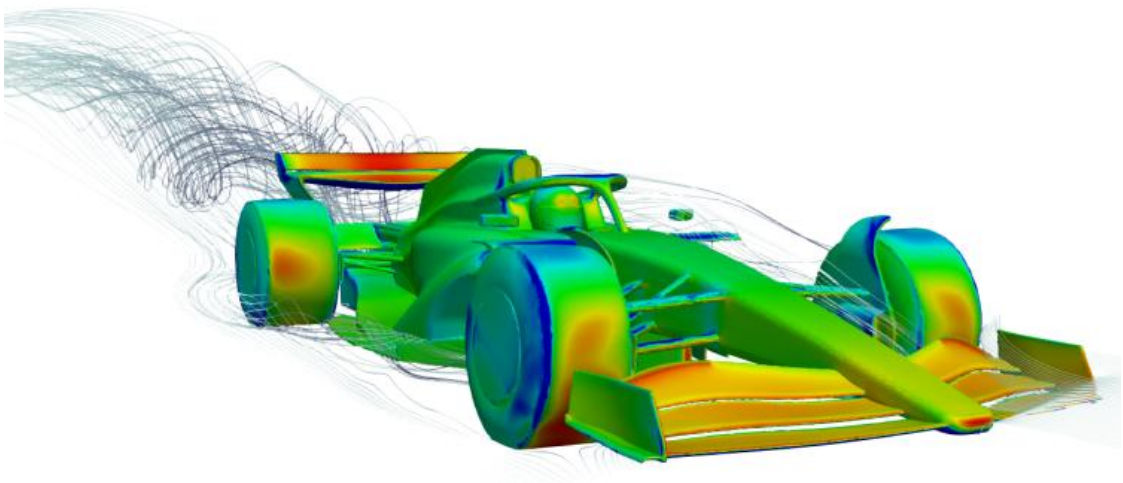
Figure 2 – Formula 1-style race car directing airflow and showing turbulent wake leaving the rear wing. Reproduced from [10].

2.5 Governing Principles of Pressure Differentials

2.5.1 Bernoulli's Principle

Bernoulli's Principle is fundamental in understanding how pressure differentials contribute to aerodynamic forces in race cars. This principle states that within a steady, incompressible flow, an increase in fluid velocity leads to a decrease in static pressure [11]. This relationship is mathematically expressed as:

$$\frac{p}{\rho} + \frac{v^2}{2} = M \tag{2}$$

Where:

- p is static pressure (Pa)
- ρ is the air density (kg/m^3)
- v is the velocity of the fluid (m/s)

Daniel Bernoulli formulated this principle in 'Hydrodynamica' (1738) and it has been widely applied in aerodynamics to explain both lift in aircraft wings and downforce in motorsport applications [12]. The inverse relationship between velocity and pressure helps to describe how aerodynamic elements influence vehicle stability and performance.

As discussed in Section 2.4, the rear wing of a race car functions by creating a pressure differential between its upper and lower surfaces. The curved bottom surface of the wing accelerates the airflow, resulting in a region of lower pressure, while the top surface experiences slower-moving air and higher pressure. The imbalance creates a new downforce to improve traction, cornering ability and braking performance.

However, Bernoulli's equation is derived under the assumptions of inviscid (frictionless) and incompressible flow, which do not account for boundary layer effects, turbulence, and flow separation. CFD simulations and wind tunnel testing are required to fully characterise these effects.

2.5.2 Newton's Third Law

Newton's Third Law states that for every action, there is an equal and opposite reaction [13]. This principle is fundamental in aerodynamics, as it explains the generation of aerodynamic forces, such as downforce, in race cars.

While Bernoulli's Principle explains the velocity-pressure relationship leading to downforce, Newton's Third Law provides an alternative perspective.

As airflow is deflected along the surface of the wing, as per Figure 1, it exerts a force on the air. According to Newton's Third Law, the air exerts an equal and opposite reaction force on the wing surface, pushing the car downward towards the ground.

This principle is particularly relevant for multi-element wings, where each element modifies the flow for the next, progressively enhancing the downward reaction force.

Qiu et al. [9] demonstrated that optimising wing setups enhanced downforce efficiency by improving airflow deflection.

In this study, Aerostrip sensors record pressure distributions on the upper and lower surface of the wing element and will quantify these pressure differentials, providing experimental validation of the reaction forces acting on the wing. By comparing sensor data with CFD simulations, this study will assess how effectively Bernoulli's Principle and Newton's Third Law apply in real-world aerodynamics, accounting for turbulence, flow separation and viscosity effects

2.6 Real-World Aerodynamic Effects

While aerodynamic principles, such as Bernoulli's Principle and Newton's Third Law, provide an understanding of pressure differentials and downforce generation, real-world aerodynamic behaviour is significantly influenced by viscosity, turbulence, and flow separation. While these effects may only result in small inefficiencies, in motorsport, tiny margins of error can lead to substantial performance losses.

2.6.1 Boundary Layers & Viscosity

Viscosity is a fluid's resistance to deformation or shear [14]. In the context of air flowing over a surface, viscosity causes layers of air to move at different velocities, generating friction. This resistance causes the fluid to 'stick' to solid surfaces and creates a velocity gradient near the wall. To simplify, a high-viscosity fluid strongly resists shear and flows slowly, while a low-viscosity fluid has less resistance and flows easily.

The interaction between a surface and airflow is described as the boundary layer, a thin region near a solid surface where viscous forces significantly influence fluid flow. The flow behaviour within this layer is directly influenced by the fluid's viscosity and velocity gradient to determine aerodynamic performance, particularly drag and flow separation [15].
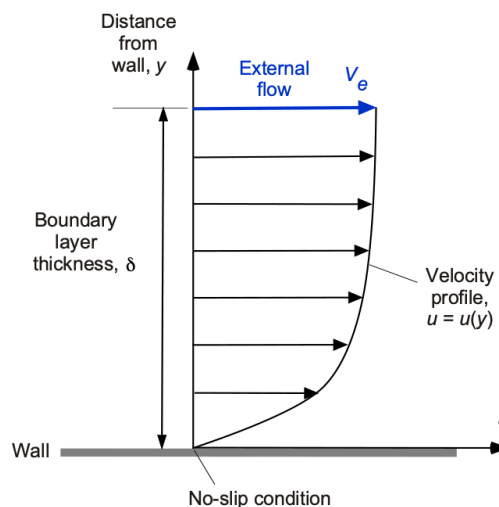
Figure 3 – Laminar flow acting in the boundary layer along the surface of a wall. Reproduced from [16].

While Bernoulli's Principle (Section 2.5.1) describes the pressure distribution on a surface that generates aerodynamic forces, it assumes an ideal, inviscid flow. In reality, viscous effects must be considered as they significantly influence the development of pressure distribution and flow attachment.

The laminar boundary layer consists of a smooth, orderly flow which minimises drag but can be impacted by flow separation under changing pressure gradients. On the other hand, a turbulent boundary layer experiences many fluctuations that allow airflow to remain attached to the surface for longer but at the cost of increased drag [15]. The transition between laminar and turbulent flow occurs at a critical Reynolds number, which is influenced by factors such as surface roughness, pressure gradients and freestream velocity. This transition is crucial in motorsport aerodynamics, where maintaining attached flow over aerodynamic surfaces, such as a wing, is vital for generating downforce and ensuring stability.
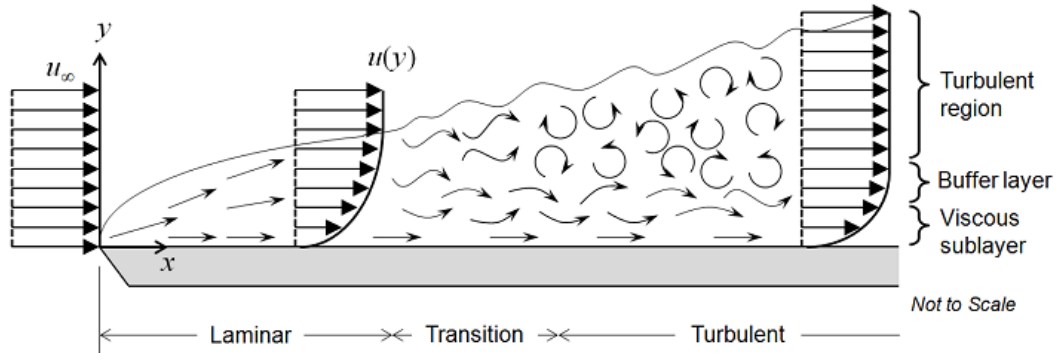
Figure 4 – Boundary layer detachment from the surface causing a transition from laminar to turbulent flow. Reproduced from [17].

In this study, Aerostrip sensor strips are used to directly measure surface pressure variations, thereby understanding flow behaviour across the rear wing. These measurements help detect the influence of viscous effects and provide valuable information on boundary layer development and potential flow separation.

2.6.2 Flow Separation
Flow separation occurs when the boundary layer detaches from the surface due to an adverse pressure gradient, which leads to turbulent air flow and increased drag [18].
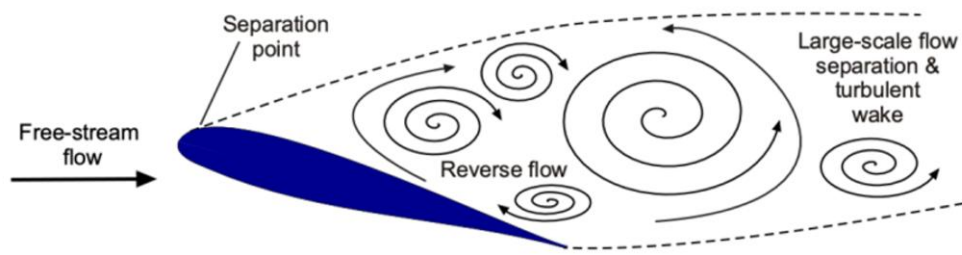
Figure 5 – Boundary layer separation on aerofoil creating a region of turbulent air. Reproduced from [16].

As airflow moves along a surface, it follows the pressure distribution set by external flow. When the pressure increases in the flow direction, the boundary layer loses momentum and can detach from the surface. Flow separation forms a low-energy recirculation zone, resulting in increased pressure drag around the system.

In motorsport applications, minimising flow separation is crucial for optimising downforce and reducing drag. Huncho [19] discusses how race car aerodynamics use multi-element wings with curved surfaces to manipulate the boundary layer and avoid separation. Formula 1-style front and rear wings are designed to re-energise the boundary layer, helping to maintain attached flow for as long as possible.

2.7 Computational Methods for Aerodynamic Validation

2.7.1 Computational Fluid Dynamics (CFD) Simulations

Computational Fluid Dynamics (CFD) is a numerical tool for solving and analysing fluid flow problems across complex surfaces and geometries. This is crucial for aerodynamic development as it enables the prediction of pressure distributions and flow structures under varying conditions without the need for physical testing. In motorsport, CFD is used for the design, evaluation and optimisation of aerodynamic components to simulate and refine performance.

CFD simulations solve the fundamental governing equations of fluid dynamics, including the Navier-Stokes equations, across a fluid domain divided into small computational cells. Fluid properties, such as pressure and velocity, are iteratively calculated in each cell over time or in steady-state conditions, allowing for the analysis of boundary layer behaviour, flow separation, and aerodynamic force generation.

In this study, CFD is used to simulate airflow over a Formula 1-style rear wing under controlled conditions, aiming to match the wind tunnel setup as closely as possible. A similar approach was adopted in a study by Kalinowski and Szczepanik [20] who optimised the shape of a racing car's front wing using CFD techniques. Their study aimed to maximise downforce-to-drag ratio by refining wing geometry in 2D and then in a 3D model. It was demonstrated that CFD-based optimisation can significantly improve aerodynamic efficiency, as results from the optimised geometry showed substantial improvements in flow behaviour and pressure distribution.

While CFD has many powerful capabilities, there are notable limitations. The accuracy of simulation results depends heavily on mesh quality, turbulence model selection, boundary conditions and physical assumptions. Physical testing and validation remain an essential method for accurately analysing airflow behaviour and this project demonstrates how Aerostrip sensor data can be used to verify the accuracy of CFD simulations in race car aerodynamic design.

2.7.2 Assumptions & Physical Models

2.7.2.1 Steady-state Simulations

In motorsport-related aerodynamic studies, steady-state CFD simulations are commonly used to evaluate pressure distributions, downforce and drag. Steady state assumes that the airflow around the vehicle remains constant over time, which is often a valid assumption when considering a constant vehicle speed operating condition.

Steady-state simulations are less computationally expensive compared to transient approaches and are suitable for comparative testing against wind tunnel results. Transient simulations can accurately capture unsteady flow structures, such as vortex shedding, but are not necessary unless highly time-dependent parameters are being investigated.

A comparative aerodynamic study by Wang et al. [21] utilised steady-state CFD simulations in Siemens STAR-CCM+ alongside wind tunnel testing for a race car wing. Results showed a close agreement in drag and downforce (within 4%), demonstrating that steady-state Reynolds-averaged Navier-Stokes (RANS) modelling is sufficient for analysing key aerodynamic behaviour of a race car wing in controlled conditions.

2.7.2.2 Incompressible Flow

Incompressible flow is a common assumption in aerodynamic CFD simulations where the flow velocity is significantly lower than the speed of sound (approximately 340 m/s in standard sea-level atmosphere [22]). This assumption simplifies the governing principles of pressure differentials and increases computational efficiency.

The Mach number (M) is defined as the ratio of the local flow velocity, V, to the local speed of sound, a [23] . This ratio is used to quantify the compressibility of a flow.

$$M = \frac{V}{a} \tag{3}$$

Flow is considered incompressible if the Mach number is less than 0.3. In this study, at a maximum velocity of 15 m/s, the Mach number M is calculated to be approximately 0.044, which is well below the threshold for compressibility effects to become significant. This assumption allows for accurate pressure predictions in external flow simulations without introducing errors related to density variation.

Incompressible flow modelling was utilised by Kalinowski and Szczepanik [20] in similar aerodynamic applications, where CFD was applied at subsonic speeds with validated results.

2.7.2.3 Boundary Conditions

In CFD, boundary conditions define how fluid interacts with the simulation domain and the direction of flow [24]. Setting boundary conditions ensures the stability and accuracy of results in aerodynamic simulations.

Typical boundary conditions include velocity inlets and pressure outlets: velocity inlets specify the incoming flow speed and direction. In contrast, pressure outlets allow the flow to exit the domain at a defined pressure.

Symmetry boundaries are commonly used to reduce the size of the domain when the flow is symmetric, helping minimise computational cost whilst maintaining accuracy. No-slip wall conditions are applied to solid surfaces to enable realistic boundary layer modelling where there is zero velocity relative to the wall [24].

The use of a moving ground boundary condition, such as a rolling road, is used in vehicle aerodynamics to simulate the relative motion between the ground and the vehicle. Kalinowski and Szczepanik [20] used a rolling road setup in their study of aerofoil performance to analyse ground effect and boundary layer developments underneath the wing.

2.7.3 Mesh Refinement

Mesh refinement is a crucial aspect of CFD simulations to improve the accuracy and stability of numerical solutions. In CFD, the domain is divided into small control volumes (or cells) over which the governing equations of fluid flow are solved. Adjusting the size, shape and distribution of these cells determines how well the simulation records changes in velocity, pressure, turbulence and boundary layer behaviour.

Refining the mesh into small and consistent cells with smooth transitions in regions of high pressure or velocity gradients, such as at the leading edge of a wing's central element, enables the solver to accurately analyse local flow features, including flow separation and sharp pressure peaks.

In the study by Kalinowski et al. [20], mesh refinement techniques were applied to their wing shapes to optimise the accuracy and outputs of their designs. Their approach involved local mesh refinement in flow regions where pressure gradients are high and the use of prism layers resolves boundary layer development. Results showed that improved mesh quality significantly enhanced prediction accuracy for pressure distribution and downforce estimation, reinforcing the importance of a good quality meshing strategy in motorsport CFD applications.

Mesh independence studies are usually conducted to ensure that simulation results converge around a measured value and do not change significantly with further mesh refinement.

2.7.4 Navier-Stokes Equations

The Navier-Stokes equations direct the motion of viscous fluid flow. In aerodynamic simulations, they are used to predict how air behaves as it interacts with surfaces such as wings or bodywork. These equations are based on the principles of mass and momentum conservation. They are solved numerically in CFD solvers, such as Siemens STAR-CCM+, to evaluate flow fields and aerodynamic forces.

2.7.4.1 Conservation of Mass

The continuity equation, which ensures mass conservation in the system [25], is expressed for incompressible flow as:

$$m = \int_{\Omega} \rho(x,t) \, dx \tag{4}$$

Where:

- m represents the mass of a finite volume Ω
- $\rho(x,t)$ represents the fluid's mass per unit volume at a point x and time t

The principles of mass conservation state that the mass contained within a material volume Ω remains constant as Ω moves with the fluid.

2.7.4.2 Conservation of Momentum

According to the principle of linear momentum conservation, the rate of change of linear momentum within a material volume is equal to the net force acting on it.

The incompressible Navier-Stokes equation describes the conservation of momentum in a Newtonian fluid [25]:

$$\frac{d}{dt} \int_{\Omega(t)} \rho u \, dx = \int_{\Omega(t)} \rho f \, dx + \int_{\partial \Omega(t)} t_n \, dS \tag{5}$$

Where:

- $\Omega(t)$ is the control volume.
- ρ is the fluid density (kg/m^3)
- u is the velocity of the fluid (m/s)
- f is the body force per unit mass (N/kg)
- t_n is the force per unit area (N/m^2) acting on the surface $\partial \Omega(t)$ with normal n

The equation (5) states that the change of momentum inside a control volume is equal to the sum of the body forces acting throughout the volume and the surface forces acting on the boundary. This follows Newton's Second Law for fluids, which states

that the rate of change of momentum of a fluid element is equal to the sum of the external forces acting upon it [26] and is the basis for the motion of fluid particles.

As described by Łukaszewicz and Kalita [25], the Navier-Stokes equations capture the forces acting within a fluid, such as pressure gradients, viscous diffusion and other external forces. Due to their nonlinearity, these equations require iterative numerical techniques such as the Finite Volume Method (FVM) for solution in CFD software.

In this study, Siemens STAR-CCM+ is used to solve the incompressible Navier-Stokes equations and describe the behaviour of the flow acting on the rear wing model, including flow attachment, separation and turbulence. This behaviour depends highly on the balance between inertial and viscous forces.

2.7.5 Reynolds Number

The Reynolds number (Re) is a fundamental parameter in fluid mechanics for characterising the nature of flow, whether it is laminar, turbulent or in transition between the two. This dimensionless number represents the ratio of inertial forces to viscous forces within a fluid, allowing for the prediction of flow behaviour around solid bodies [27].

$$Re = \frac{\rho U D}{\mu} \tag{6}$$

Where:

- ρ is the fluid density (kg/m^3)
- U is the freestream velocity (m/s)
- D is the characteristic length (wing chord, m)
- μ is the dynamic viscosity of the fluid (Pa·s)

The Reynolds number influences boundary layer development, drag and pressure distribution, all of which affect overall aerodynamic efficiency. A low Reynolds number typically corresponds to laminar flow, whereas higher Reynolds numbers can lead to turbulence and increased mixing.

In this study, Reynolds number calculations were used to match the test conditions in CFD simulations and wind tunnel experiments. Real-world data collected using Aerostrip sensors enable the comparison of flow behaviour at different Reynolds numbers and the assessment of the accuracy of CFD simulations. Comparing experimental and simulated data can determine whether transitional or turbulent features are accurately captured in the generated model.

2.7.6 Turbulence Modelling

Turbulence Modelling is essential in CFD simulations, particularly when studying high-speed flow aerodynamics in a motorsport environment. Turbulence is a chaotic, three-dimensional and time-dependent motion of fluid particles that occurs at high Reynolds numbers, causing fluctuations in velocity, pressure and vorticity. A visual

representation of oscillations developing in the boundary layer and laminar flow transitioning to turbulent flow is shown in Figure 4 (Section 2.6.1).

The most common turbulence approximation is the Reynolds-averaged Navier-Stokes (RANS) approach. RANS models solve time-averaged versions of the Navier-Stokes equations and introduce turbulence effects through additional equations. These models are widely used in industrial aerodynamic applications as they offer a practical balance between computational cost and prediction accuracy. However, for automotive flows, they have known limitations when predicting complex flow features such as lift and drag [28].

In this study, three commonly used RANS turbulence models were selected to assess their ability to simulate flow over the Formula 1-style rear wing:

2.7.6.1   k-ω SST (Shear Stress Transport) Model

The k-ω SST model is well-suited for flows with unpredictable pressure gradients and separation. It combines the standard k-ω model and the k-ε model to produce reasonable stability and accuracy when predicting flows with boundary layer separation [29]. The k-ω SST model serves as the baseline for this project.

2.7.6.2   k-ε Model

The k-ε model is one of the most widely used models in industrial CFD due to its simplicity and robustness. This model solves two transport equations for turbulence kinetic energy (k) and dissipation rate (ε) and performs well in free-shear flows [29]. However, its near-wall performance is limited and therefore, struggles with predicting flow separation in the presence of pressure gradients.

2.7.6.3   Spalart-Allmaras Model

The Spalart-Allmaras (SA) model is a one-equation eddy-viscosity turbulence model initially developed for aerospace applications, particularly for predicting turbulent flows around aerofoils and wings. However, as discussed by Kostić [30], while the SA model performs well in regions of attached flow, it can show limitations when capturing complex flow behaviour such as separation. The SA model is relevant for this study as the rear wing domain used in simulations features similar flow behaviour and this model can be critically assessed to understand its predictive capabilities.

The comparison of differing turbulence models was motivated by findings from Zhang et al. [28], who evaluated various turbulence models, including k-ω SST, standard k-ε and the hybrid Detached Eddy Simulation (DES), in their study of how turbulence modelling affects CFD predictions. Their results confirmed that while all RANS turbulence models captured general aerodynamic trends, each model had specific strengths and weaknesses depending on the flow region. It was discovered that the k-ω SST model was most reliable for analysing boundary layer behaviour and drag coefficients, while the standard k-ε model struggled in wake prediction. The SA model was not featured in this analysis but will be used in this study to understand its behaviour and performance when predicting airflow behaviour.

2.8 Data Collection

2.8.1 Wind Tunnel Testing

Wind tunnel testing is a fundamental method in experimental aerodynamics. It is commonly used to evaluate flow behaviour, pressure distribution and aerodynamic forces on scaled or full-size models in a controlled environment. In motorsport, wind tunnel facilities are used to validate computational models and optimise aerodynamic performance. Conducting wind tunnel pressure measurements helps to understand real-world flow conditions that may not be accurately captured in CFD simulations.

Previously mentioned studies by Zhang et al. [1] and Subramanian et al. [2] have demonstrated the effectiveness of wind tunnels in characterising aerodynamic performance while validating the accuracy of the Aerostrip sensor. These studies demonstrate the value of wind tunnel environments for precise control of flow velocity and test configurations, ensuring that pressure measurements can be directly compared with CFD predictions.

The findings by Wang et al. [21], as previously discussed in Section 2.72, further support the reliability of wind tunnel testing in validating CFD simulations. Their use of a consistent test environment and aerodynamic model provided high-quality results that closely aligned with computational data. The studies above strongly support the use of wind tunnel testing for similar style projects to provide consistent, high-quality data when assessing real-world airflow conditions. The accuracy of numerical models will be directly compared to understand complex aerodynamic behaviour acting on the rear wing of USM's race car, such as flow separation, boundary layer behaviour and turbulent wake structures.

2.9 Aerodynamic Development in Motorsport

While wind tunnels remain essential for aerodynamic validation, their use in motorsport can be limited by restrictions such as cost, complexity and computational time.

Aerodynamic advancements and testing are heavily restricted by the Fédération Internationale de l'Automobile (FIA) regulations, which are designed to reduce excessive performance advantages and ensure a level playing field, thereby promoting overtaking and on-track competitiveness. Over the past two decades, regulatory changes have progressively limited the type and extent of aerodynamic testing that Formula 1 teams can conduct. This study analyses the aerodynamic performance of a Formula 1-style rear wing and therefore considers how aerodynamic development is undertaken within Formula 1.

Rule changes in 2009 significantly reduced aerodynamic freedom by simplifying wing geometry and introducing strict dimensional constraints [31]. These restrictions were further updated in 2014, limiting in-season wind tunnel testing and capping the hours available for CFD simulations for team development. The introduction of a budget cap

in 2021 also emphasised the need for efficiency and resource management in aerodynamic testing.

As of 2025, aerodynamic development is further constrained under the FIA Sporting Regulations, particularly in Appendix 7: Aerodynamic Testing Restrictions (ATR) [32]. This section outlines the strict limits on wind tunnel use, CFD hours and model configurations. These rules are in place to prevent dominant teams from gaining a further advantage by exploiting simulation resources or conducting excessive testing while promoting efficiency and technical creativity within the regulations.

Despite these constraints, wind tunnel and CFD testing remains a critical tool in aerodynamic development. In a study by Nakagawa et al. [33], highly detailed aerodynamic testing was conducted using PIV to highlight the challenges of aerodynamic development within FIA regulations. Their study highlights the complexity and cost of identifying flow structures, such as vortices and surface pressure distributions, on full-scale or near-full-scale Formula 1 models.

In an increasingly regulated and costly industry, there is growing interest in aerodynamic measurement tools that are efficient, reusable and compliant with regulations. Within this context, the Aerostrip sensor system presents a promising alternative. Its ability to capture high-resolution surface pressure data without intrusive installation makes it particularly suited for motorsport developments.

3   Design & Experimental Integration

3.1   Rear Wing Setup

The multi-element rear wing used in the wind tunnel experiment consists of five aerodynamic elements:
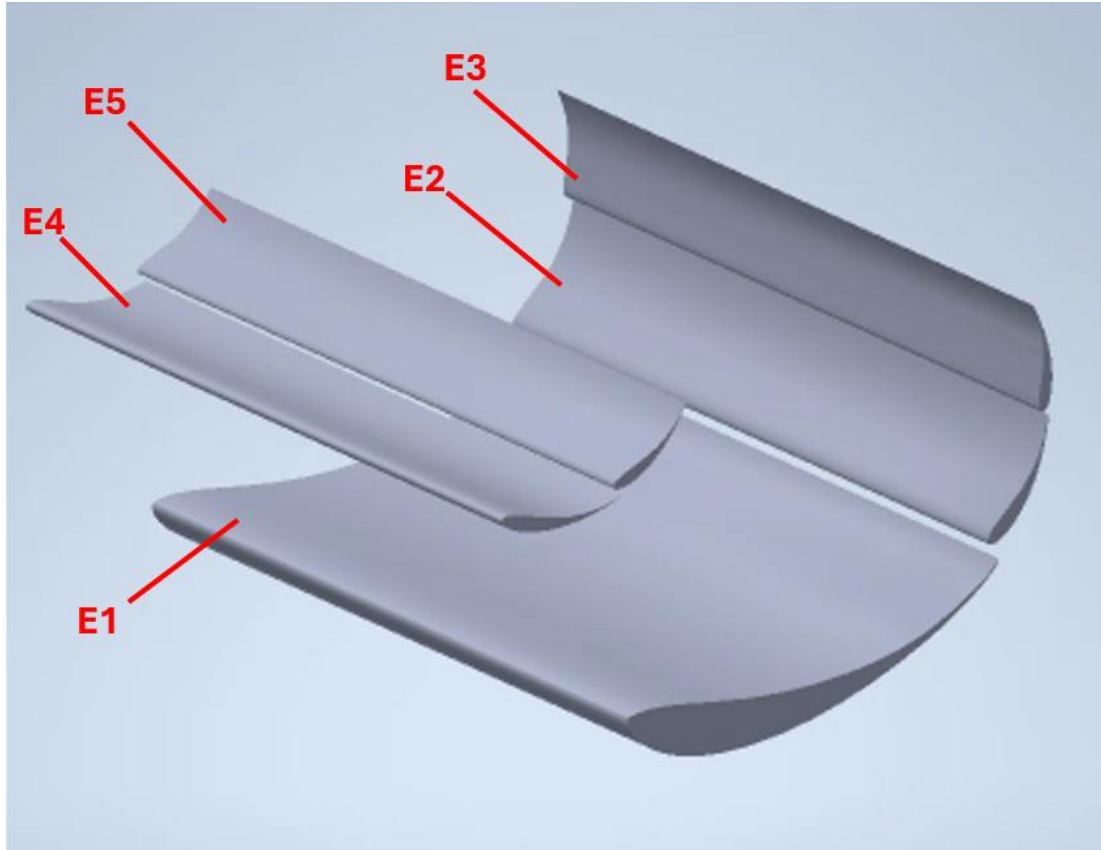
Figure 6 - Rear wing element layout consisting of 5 key elements that direct airflow. Endplates are removed from the geometry for clarity.

The largest element, E1, is the primary focus of this study due to its dominant role in generating downforce. Wing element 1 (E1) has a low aspect ratio (AR) with a rectangular platform (950 mm wingspan x 496 mm chord) and a curved aerofoil profile.

The aspect ratio (AR) of E1 is calculated as **1.92**. This low aspect ratio, combined with a cambered cross-section profile, makes it particularly effective for generating high downforce in motorsport conditions. The geometry is well-suited for evaluating surface pressure distributions, with strong gradients expected near the leading edge and mid-chord region of the aerofoil.

To analyse pressure distribution, Aerostrip sensors are installed at the quarter-span locations on both the upper and lower surfaces of E1. This positioning allows for a detailed investigation of chordwise airflow behaviour whilst minimising endplate interference.

Figure 7 – Aerostrip sensors installed along the chord of E1's upper surface at quarter-span. Sensors are installed with elements near the leading edge of the aerofoil.
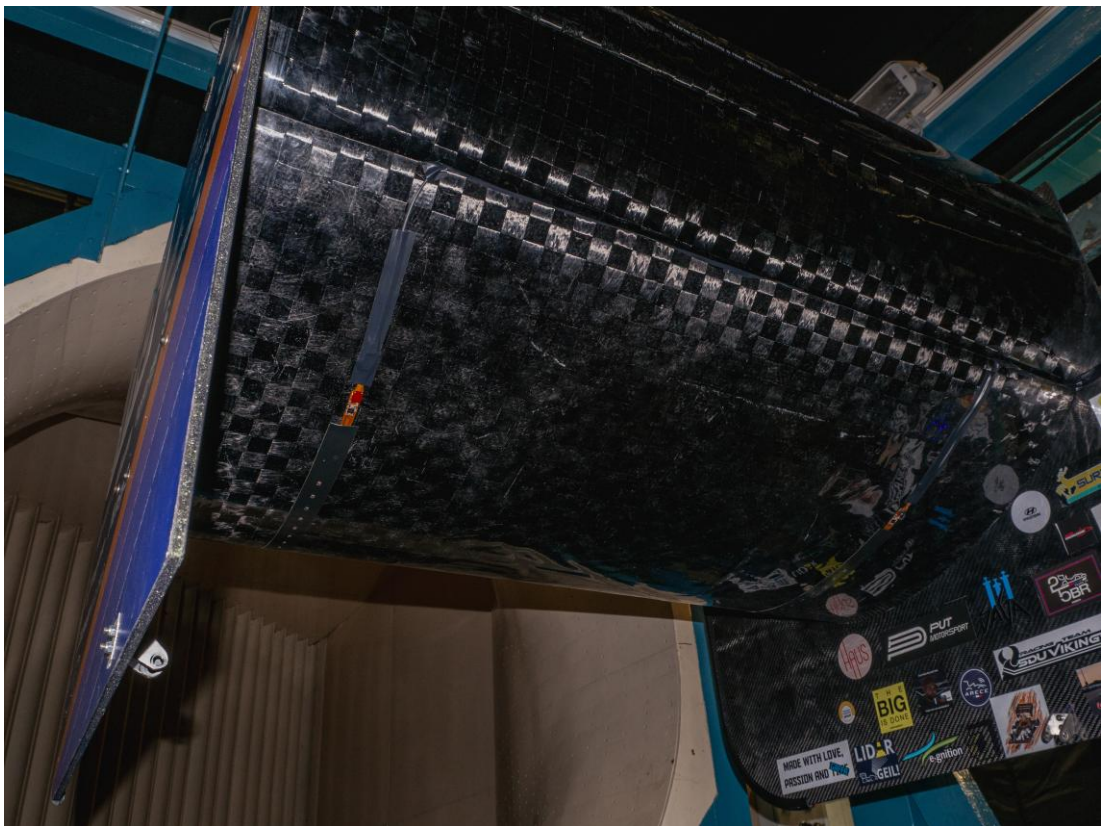
Figure 8 - Aerostrip sensors installed along the chord of E1's lower surface at quarter-span. Sensors are installed with elements near the leading edge of the aerofoil.

To accommodate the wind tunnel mounting system, the secondary arrays (E4 and E5) are removed. This modification enables the integration of a custom plate and bracket assembly that secures the wing to a slim steel beam mounted from the wind tunnel's ceiling. A top-mounted setup is chosen to minimise airflow disruption, as a bottom-mounted structure would introduce more interference in the flow field. Additionally, the upper surface of E1 contains four pre-existing fixings, making this mounting approach the most structurally viable option.

To ensure that CFD simulations and wind tunnel experiments are directly comparable, the plate, bracket and steel beam are incorporated into the simulations alongside the removal of E4 and E5. This approach eliminates inconsistencies between numerical and experimental data, allowing for more accurate validation of pressure measurements and aerodynamic performance.

Despite efforts to minimise interference, the presence of the central steel beam may introduce some localised airflow disruption due to nonidealities in the material. However, since Aerostrip sensor strips are positioned at quarter-span along E1, any disturbances near the centre should not significantly impact recorded pressure data.

The rear wing assembly features large endplates on each side, which help control wingtip vortices and enhance aerodynamic efficiency. Unlike some motorsport wings that feature adjustable flaps, the elements in this wing assembly are fixed and do not allow for variations in the angle of attack, which is the angle at which the aerofoil passes through the air. While adjustable flaps could provide greater tuning flexibility, the current wing setup is designed alongside CFD simulations to maximise aerodynamic efficiency.

Aerostrip sensors are installed at quarter-span on both the upper and lower surfaces of E1 to analyse pressure distribution along opposite chord lengths.

The pressure variation across the wingspan will also be assessed on each side of the aerofoil. Using the percentage difference equation (7), airflow behaviour and distribution can be evaluated to understand how air separates after splitting at E1's leading edge.

$$Percentage\ Difference\ (\%) = \left(\frac{|A - B|}{\left(\frac{A + B}{2} \right)} \right) * 100 \tag{7}$$

Where:

- A is the measured pressure at one quarter-span Aerostrip
- B is the measured pressure at a differing quarter-span Aerostrip

By recording pressure variations across E1 using Aerostrip sensors, airflow behaviour can be examined as it interacts with the rear wing, including factors such as flow

separation, pressure sensitivity and the aerodynamic forces acting on the wing assembly.

3.2   Mounting System Design

To securely mount the rear wing in the wind tunnel for controlled aerodynamic testing, a custom bracket assembly is designed and manufactured. This structure is connected to a vertical steel beam suspended from the wind tunnel ceiling, ensuring stable positioning of the wing relative to the freestream flow.

The bracket is designed to connect to four existing mounting points on the upper surface of E1, originally intended for wing attachment to the vehicle body. A tab and plate system is created in Autodesk Inventor 2024 and manufactured from 3mm thick aluminium using waterjet cutting to ensure precision and clean edges.
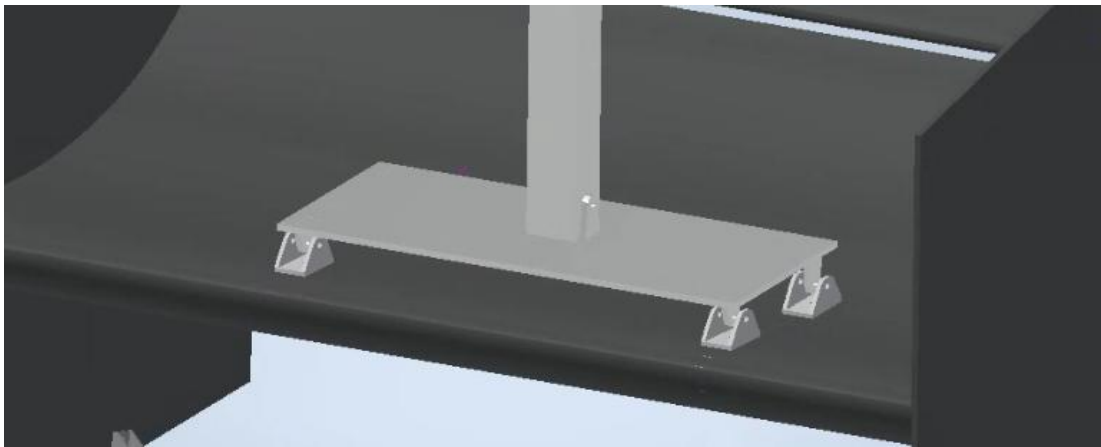
Figure 9 – Custom-designed mounting structure with tabs, plate and beam secured to the rear wing model.

Due to the curved geometry of the wing array, smaller tabs (approximately 27 mm in height) are designed for the front-facing inserts of the mounting plate near the leading edge of the wing. These front-facing tabs are made to match the wing's curved profile, maintain the correct pitch relative to airflow and ensure the test orientation matches both real-world and CFD test configurations.

Larger tabs are created for the rear-facing inserts of the mounting plate near the trailing edge of E1 (approximately 40 mm in height).

After manufacture, the tabs are welded into the mounting plate inserts. The bracket is secured to the wing by bolting through the pre-existing fixings to provide a direct and secure connection. Detailed drawings of both tab designs and the mounting plate are illustrated in Appendix A.

To join the steel beam and the aluminium plate together, a smaller secondary plate is bolted to the top surface of the main plate. This plate provided a rigid base for welding the vertical support beam to the surface. The smaller plate was not initially incorporated into designs but is deemed necessary to conduct secure welding attachment.

Four fixed mounting points on the bracket eliminated any unwanted movement or rotation of the wing under aerodynamic load. This rigidity is essential for maintaining repeatability and accuracy across all test conditions.

Earlier versions during the design phase did not include the small connector plate and relied on a single through-bolt between two welded tabs to secure the plate to the beam. However, this approach introduced a pivot point which allowed the wing to rotate under load, compromising the test setup. Incorporating multidirectional fixings significantly improved the structural integrity and prevented any rotation.

Through the design process, a greater understanding of force distribution and mechanical restraint was developed. The final bracket assembly proved effective in resisting aerodynamic forces and maintaining consistent test conditions across repeated runs.

3.3   Experimental Setup

To ensure reliable and consistent measurements, the wing is carefully positioned within the wind tunnel's working section for testing at two different wind speeds. This setup enabled the investigation of the Reynolds number effect on pressure behaviour and flow characteristics, supporting a direct comparison with numerical solutions.

3.3.1   Wind Tunnel Setup

The tests are performed in an open-loop wind tunnel with a working section of 1.5 m x 1.5 m x 2 m. This ensured a uniform freestream velocity across the model. The rear wing was mounted using the custom bracket and plate assembly and positioned to intersect the centreline of the airflow. The flow centreline is determined by considering the circular section of the nozzle. The mounting system ensured that the wing remained aligned with the free-stream flow throughout testing to maintain consistency with CFD boundary conditions.
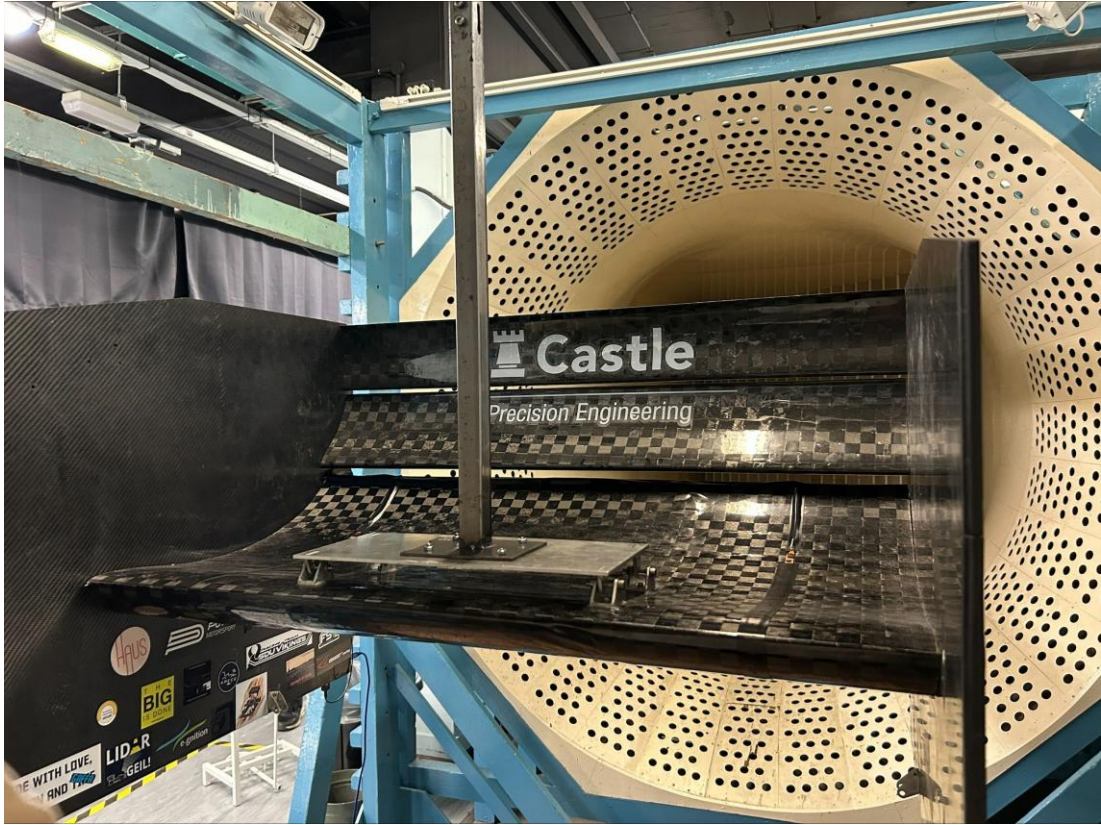
Figure 12 - Rear Wing and Mounting Structure Assembly Secured in Open-Loop Wind Tunnel. Aerostrip sensors are installed at each quarter-span on the upper and lower surface of E1.

To minimise flow disturbances, the wing is installed approximately one-third of the way downstream from the nozzle exit into the test section. This positioning reduces the influence of the shear layer generated at the nozzle boundary, ensuring stability in airflow across the wing.

3.3.2 Test Conditions & Reynolds Number

Wind tunnel tests are conducted at two different freestream velocities: 10 m/s and 15 m/s, allowing for an analysis of the effects of Reynolds number on flow behaviour and aerodynamic performance. These speeds are selected to simulate low to moderate operating conditions, ensuring that airflow remains within the turbulent regime relevant to motorsport applications. Velocity in the wind tunnel is validated during testing using a digital anemometer (HoldPeak HP-866B).

Reynolds numbers are calculated based on equation 6 (Section 2.7.5), with the following constants:

- Air density, ρ: 1.225 kg/m^3 (ISA standard [34])
- Dynamic viscosity, μ: 1.81 x 10^{-5} Pa·s
- Characteristic length, D: 496 mm (chord length of E1)

The resulting Reynolds numbers for each test velocity are:

- $U = 10$ m/s: **Re = 3.35 x 10^5**
- $U = 15$ m/s: **Re = 5.03 x 10^5**

These values confirm that the flow over the rear wing operates within a turbulent regime, which is essential for capturing boundary layer development, flow separation and aerodynamic forces. Ensuring similarity between the Reynolds numbers in the wind tunnel and CFD simulations supports the accurate validation of the computational model and turbulence modelling strategies used in this study.

3.3.3   Sensor Configuration

The rear wing was installed with Aerostrip sensor strips at the quarter-span locations of the upper and lower surfaces of E1. Surface pressure measurements were conducted using two different sensor pitches:

- 20 mm element pitch
- 8mm element pitch

The two sensor configurations are used in this study for different measurement objectives. The 20 mm pitch element strips are positioned along the chord length of E1 on opposing surfaces, covering a range from 20 mm to 240 mm. This setup enables the analysis of large-scale aerodynamic trends and the measurement of surface pressure distribution along the aerofoil to evaluate aerodynamic properties such as downforce generation, boundary layer behaviour, and flow separation.

The 8 mm pitch elements are utilised for fine-resolution analysis to capture pressure peaks as airflow splits at the leading edge of E1 between the upper and lower surface along the boundary layer.
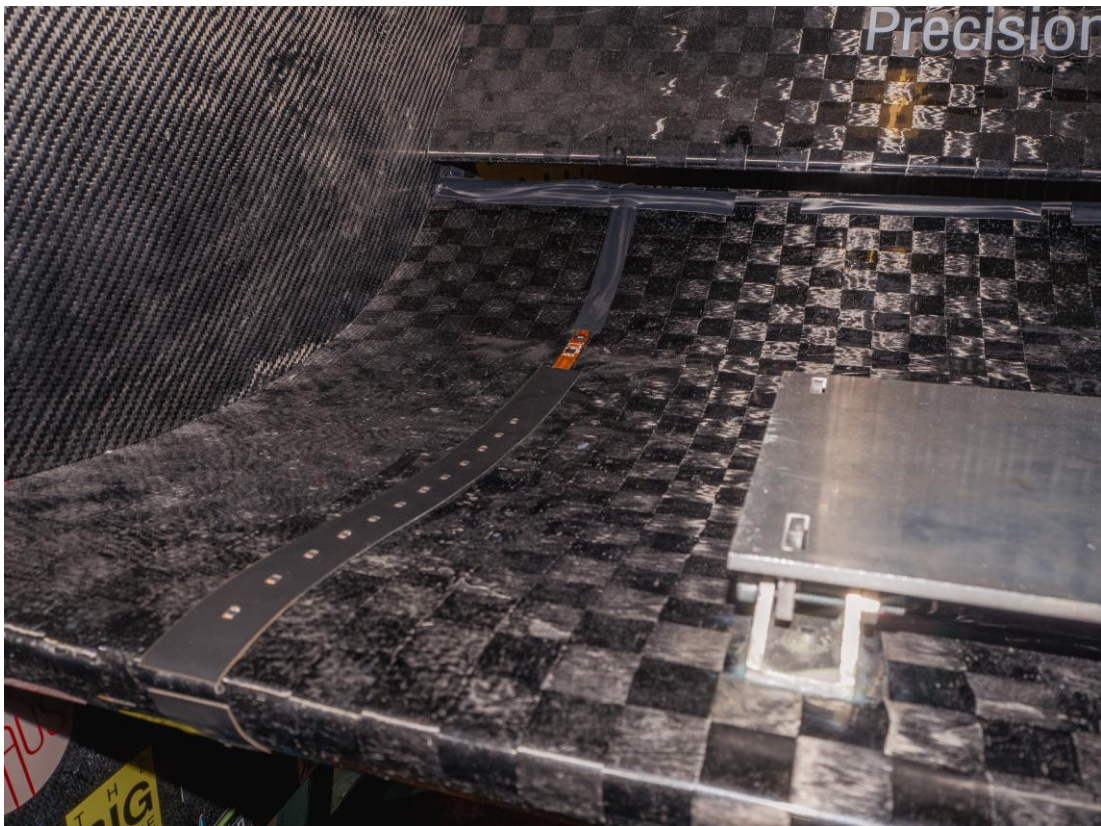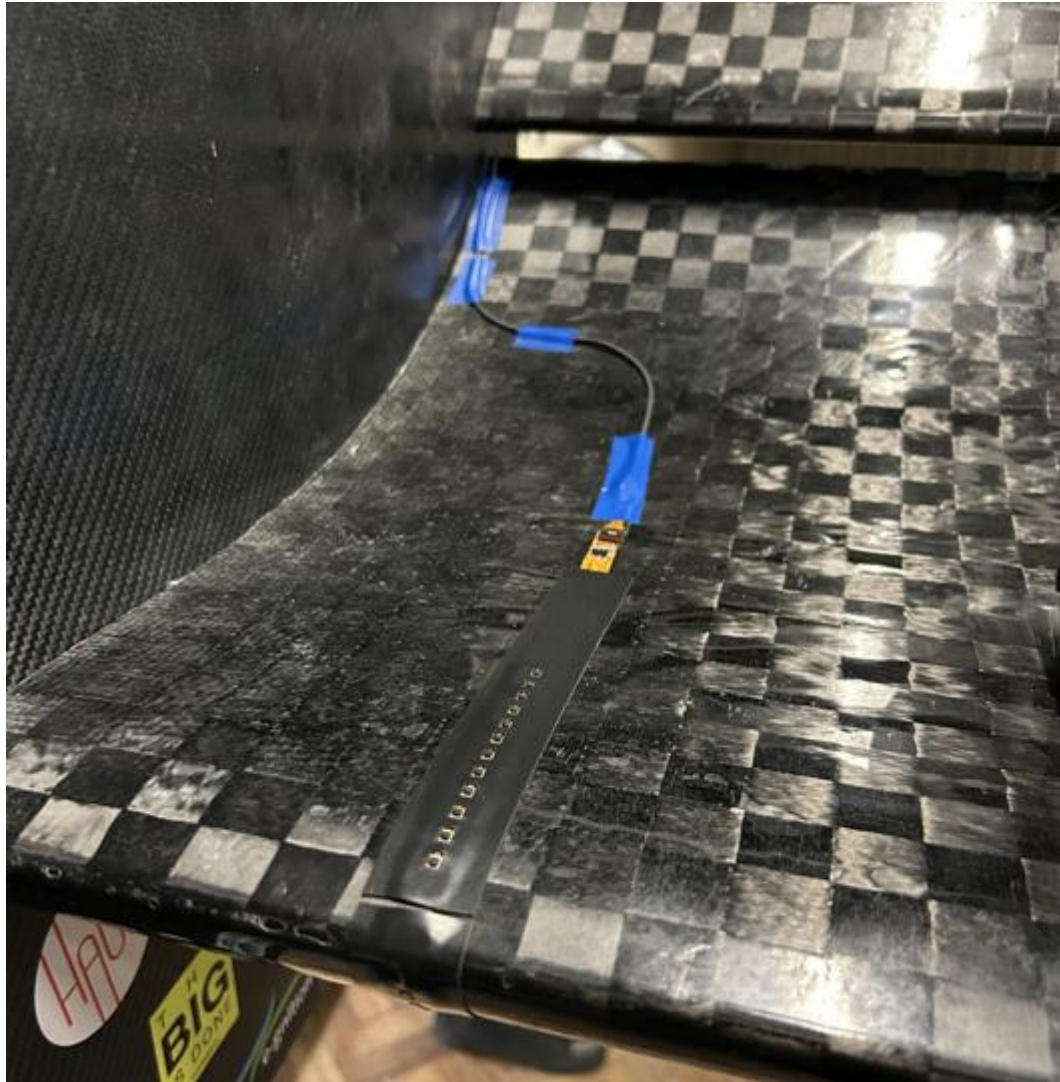
Figure 14 - 8 mm pitch element Aerostrip installed at quarter-span on E1. The first element is installed 20 mm along the chord on the upper surface and at the leading edge (0 mm) on the lower surface. It should be noted that cable management has not been performed at this stage.

3.3.4 Cable Management & Airflow Optimisation

Minimising interference with the freestream airflow is an essential consideration during wind tunnel testing. Effective cable management around the wing assembly was necessary to reduce the impact of external hardware on aerodynamic behaviour.

Aerostrip sensors are installed at the quarter-span positions on both the upper and lower surfaces of E1, with four sensors installed in total. However, with multiple installations, additional cable management is required along the chord and wingspan.

These cables could introduce potential disruptions to the airflow exiting the wing and could affect downstream interactions with other elements in the array.

To mitigate this potential interference, additional tests are conducted using only one Aerostrip sensor on each surface of E1. This setup significantly reduced cabling across the surface, allowing for cleaner airflow downstream.

The DAQ microcontroller, where pressure data from the sensors is received, is mounted flush against the outer face of the endplate to minimise aerodynamic effects. This mounting strategy is considered more suitable than cables hanging vertically into the freestream region and introducing perpendicular surfaces to the flow.

This refined setup reduces physical obstruction in the working section and ensures that the collected surface pressure data has minimal aerodynamic interference compared to simulated predictions.

3.4   Pressure Differential & Downforce Calculation

To assess the aerodynamic performance of the rear wing, surface pressure data is collected using the Aerostrip sensors positioned on the upper and lower surfaces of E1. From the recorded pressure values at each corresponding pressure pair, a local pressure difference (ΔP) is calculated. These localised pressure differentials provide insight into the distribution of aerodynamic loading across the aerofoil.

Each pressure differential is converted into a local force using the basic pressure-force-area relationship:

$$F_{local} = \Delta P \cdot A \tag{8}$$

Where:

- ΔP is the pressure difference between the upper and lower surfaces (Pa).
- A is the effective area of the sensor element, taken as 500 mm^2 (25 mm width · 20 mm pitch).

The total downforce generated by the wing is then estimated by scaling the sum of local forces across the full span of the wing

$$F_D = \sum F_{local} \cdot \frac{950}{25} \tag{9}$$

Here, 950 mm represents the total wingspan of E1 and 25 mm is the width covered by the sensor strip. This linear scaling assumes a relatively uniform spanwise pressure distribution and a symmetric wing setup.

To support the use of this 2D strip-based force estimation method, the wing's aspect ratio (AR) [35] is calculated as:

$$AR = \frac{s^2}{A} = \frac{950^2}{950 \cdot 496} = 1.91 \tag{10}$$

This low aspect ratio (1.91), typical in motorsport rear wings, supports the assumption that flow characteristics are predominantly 2D. This allows for simplified chordwise pressure integration.

Although the wing has a finite thickness, it is not explicitly accounted for in the downforce, F_D, calculation. Since pressure acts perpendicular to the surface and is integrated over the projected area, the thickness has minimal influence on the resulting force vector. Additionally, the calculation does not aim to resolve tangential shear stresses or other 3D effects, which are negligible in comparison to pressure-driven downforce at the tested Reynolds number values.

While the CFD analysis predicts surface pressure data across the entire chord of the wing, the experimental calculation is limited to the length of the Aerostrip sensor. For this reason, only data measured from equivalent chordwise positions are used to compare to experimental and numerical downforce predictions. While this method does not cover full-chord pressure variation, it provides a reliable and accessible means of estimating downforce and validating aerodynamic performance using physical pressure measurements.

3.5   Data Collection

Surface pressure data is collected using PPS's Chameleon software, which receives and displays data in real time from the DAQ microcontroller linked to Aerostrip sensors. The system provides a live visual interface showing the pressure values at each sensor location. The Chameleon interface is shown:
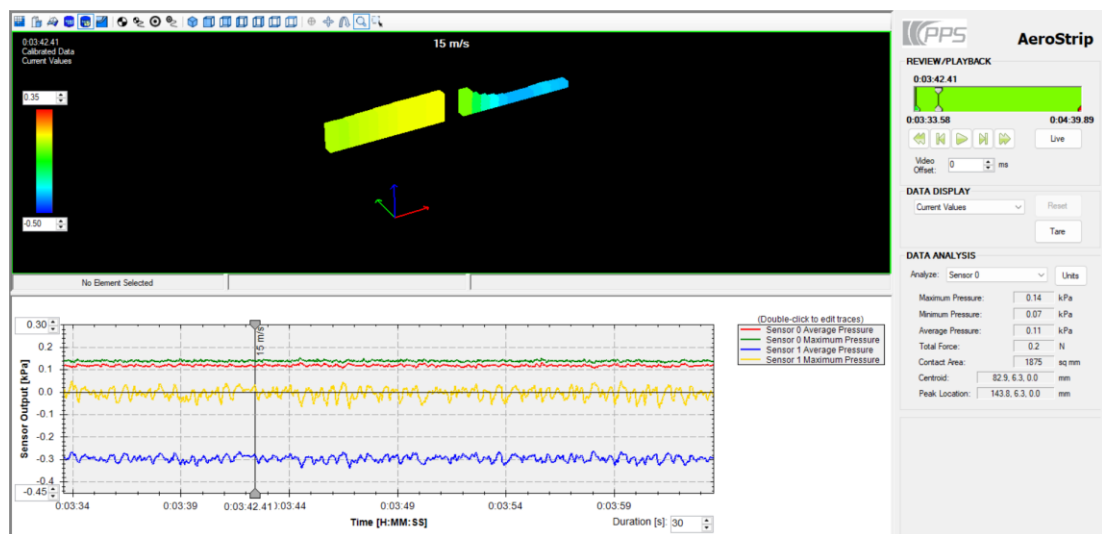
Figure 16 - Chameleon software interface showing 3D pressure distribution between sensors as well as live pressure data (kPa).

For every test, pressure readings are recorded at a sampling frequency of 200 Hz, corresponding to one data point every 0.005 seconds. The pressure value for each sensor is displayed against time, allowing the user to observe the stability of the readings during the test period.

Before a steady pressure trend is established, a buffer of approximately 10 seconds is applied within the software to isolate stable data and exclude any transient readings that may occur at the start of recording. The average pressure value for each sensor is then calculated across this buffered window (60 seconds).

After each test, the raw time-series data was exported into .csv format, including pressure values for each individual element. These datasets are later used for post-processing in Microsoft Excel to evaluate pressure differentials and perform downforce calculations.

3.6 Computational Fluid Dynamics (CFD) Simulations

To replicate wind tunnel conditions and analyse aerodynamic performance, CFD simulations are conducted using Siemens STAR-CCM+. The CFD model included the rear wing and mounting structure assembly:
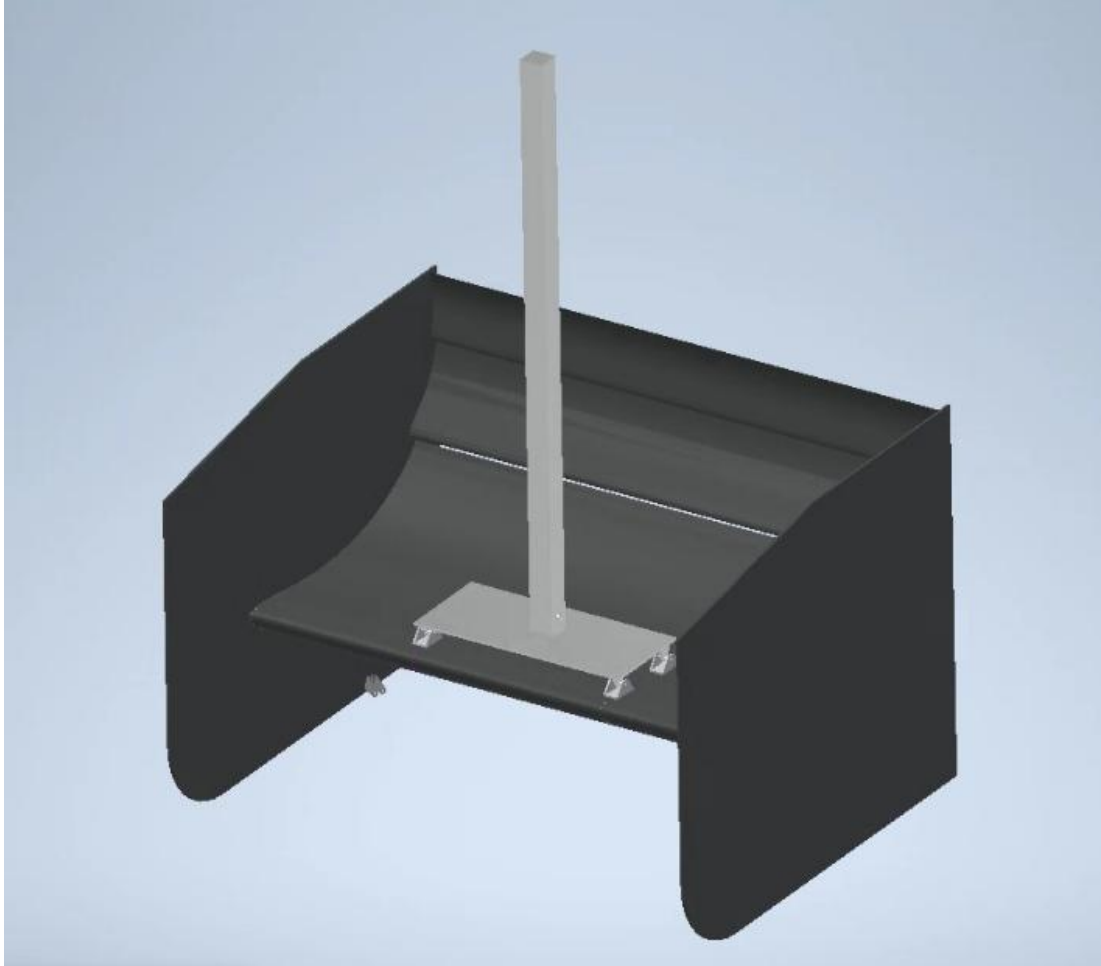
Figure 17 – Rear wing and custom bracket CFD model for simulations. Matching wind tunnel model and setup.

The simulated geometry includes the main wing element (E1), additional pre-existing wing elements (E2 and E3), large end plates and the custom-designed mounting structure (Section 3.2). The simulations are configured to closely match the physical setup of the wing tests for direct comparison with experimental results, including the removal of secondary elements (E4 and E5) to ensure consistency between experimental and numerical data.

3.6.1 Domain and Boundary Conditions

A half-car model is used to reduce computational resources, with symmetry planes applied along the longitudinal midplane. The computational domain measures 32 m in length, 7 m in height and 7 m in width, resulting in a blockage ratio of 1.22%. The model is positioned 9 m downstream of the inlet to allow flow development and reduce entrance effects.

The domain boundaries are as follows:

- **Velocity inlet** set to 15 m/s with a uniform flow profile.
- **Pressure outlet** set to ambient static pressure.
- **Rolling road floor** to replicate on-track conditions.
- **Symmetry plane walls** to simulate an unbounded external flow.

No-slip boundary conditions are applied to all solid surfaces, including the entire wing and mounting structure, with wall treatment enabled to resolve near-wall flows.

3.6.2   Meshing Strategy

A polyhedral mesh is applied with prism layers near all solid boundaries to assess boundary layer development. Prism layers are generated to resolve velocity and pressure gradients close to the surface.

To improve accuracy in regions of high expected gradients and around sharp curves, mesh refinement is applied near the wing surface. This region utilised a 30% reduced base size and a minimum cell size equivalent to 5% of the global base size. The global base size is set to 17 mm.

A formal mesh independence study was conducted in line with USM's previous rear wing CFD setup. The CFD model and surrounding region used 3,212,715 cells to converge pressure distribution outputs with the best computational efficiency.

3.6.3   Turbulence Model

A k-ω SST turbulence model is selected as the initial choice for this study due to its common use in aerodynamic simulations and its proven ability to handle boundary layer separation. To assess the influence of turbulence model selection on pressure distribution accuracy, additional simulations will use Spalart-Allarmas and k-ε turbulence models at wind speeds of 10 and 15 m/s.

By comparing the results across these models, the study aims to evaluate the predictive performance of differing turbulence model simulations in relation to experimental data. This analysis looks to identify which model offers the best compromise between accuracy and computational efficiency for motorsport aerodynamic applications. By validating various turbulence models, the future selection of simulation setups for USM is verified, which will contribute to refining their aerodynamic simulation workflow.

3.6.4   Physical Assumptions

Simulations are run in steady state, assuming incompressible, subsonic flow. Compressibility effects are neglected since the flow velocity (a maximum of 15 m/s) remains well below the critical threshold of 100 m/s. The energy equation is not considered and the working fluid is treated as an ideal gas with constant density.

Gravity, buoyancy forces and aeroelastic effects are neglected due to their negligible influence at this scale. The wing and mounting structure are assumed to be rigid and stationary under aerodynamic loading.

4   Testing Methods & Results

4.1   Wind Tunnel Testing

Surface pressure data was collected using Aerostrip sensors installed on the upper and lower surfaces of the rear wing element, E1, during wind tunnel experiments. Sensors are placed at quarter-span on both surfaces, allowing for a detailed analysis of chordwise pressure trends. Local pressure measurements enable the computation and comparison of downforce values with those obtained from CFD simulations.

To ensure consistent and reliable results, multiple tests are conducted at freestream velocities of 10 m/s and 15 m/s, corresponding to Reynolds numbers 3.35 x 10^5 and 5.05 x 10^5, respectively. Data is collected over a 60-second timeframe, after an inserted buffer at the start of recordings to prevent any transient effects, with pressure readings recorded by each sensor element every 0.005 seconds. The time-averaged mean pressure from each sensing element is used to calculate steady state values.

Prior to each test, relative pressure is checked to confirm sensor baseline and ambient temperature conditions. The test environment was maintained to replicate ideal flow conditions, with the wing aligned to the nozzle centreline for accurate flow distribution across the setup.

4.1.1   20 mm Pitch Sensors

4.1.1.1   Methods

The 20 mm pitch configuration consisted of 12 sensing elements evenly spaced along the chord of E1, covering a range from 20 mm to 240 mm. This setup was selected to capture large-scale aerodynamic behaviour and identify key pressure distribution patterns across the aerofoil.

Due to the coarser resolution, this configuration is best suited for illustrating overall trends in surface pressure distribution and calculating total downforce. Pressure data collected from each sensor element was used to compute local pressure differentials between the upper and lower surfaces of E1. These differentials were then used to estimate the corresponding downforce values acting on the entire wingspan.

This configuration provided the baseline dataset for comparison with CFD simulations, enabling the evaluation of pressure trends, distribution gradients and force estimation accuracy.

4.1.1.2   10 m/s Freestream Velocity Results

At a wind speed of 10 m/s, the pressure data shows a clear differential between the upper and lower surfaces of the wing. As expected, the bottom surface, experiencing faster airflow, measured significantly lower pressures, while the upper surface maintained a higher pressure distribution across the measured chord length. These results align with expected aerodynamic behaviour for downforce generation. A significant pressure increase was noted at the mid-chord region of the wing's lower surface:

Figure 18 – 20 mm pitch element Aerostrip measurement of pressure distribution acting on E1 at 10 m/s freestream velocity.

Using the computed pressure differentials from each sensor pair, local force contributions were summed and scaled, resulting in a total downforce of 48.562 N.

$$F_D = \sum F_{local} \cdot \frac{950}{25} = \mathbf{48.562 \ N}$$

This result serves as the basis for comparison with CFD simulations, providing insight into the pressure-driven aerodynamic loading on the wing at this flow condition.

4.1.1.3   15 m/s Freestream Velocity Results

Increasing the freestream velocity to 15 m/s amplified the magnitude of the pressure differential across the wing whilst maintaining a similar distribution trend observed at lower speeds. As with the 10 m/s test, a consistent pressure rise was noted along the boundary layer of E1's lower surface, particularly in the mid-chord region.

The overall shape of the pressure distribution across E1 remained comparable to the lower velocity case, confirming that the aerodynamic behaviour scales predictably with increased flow speed.
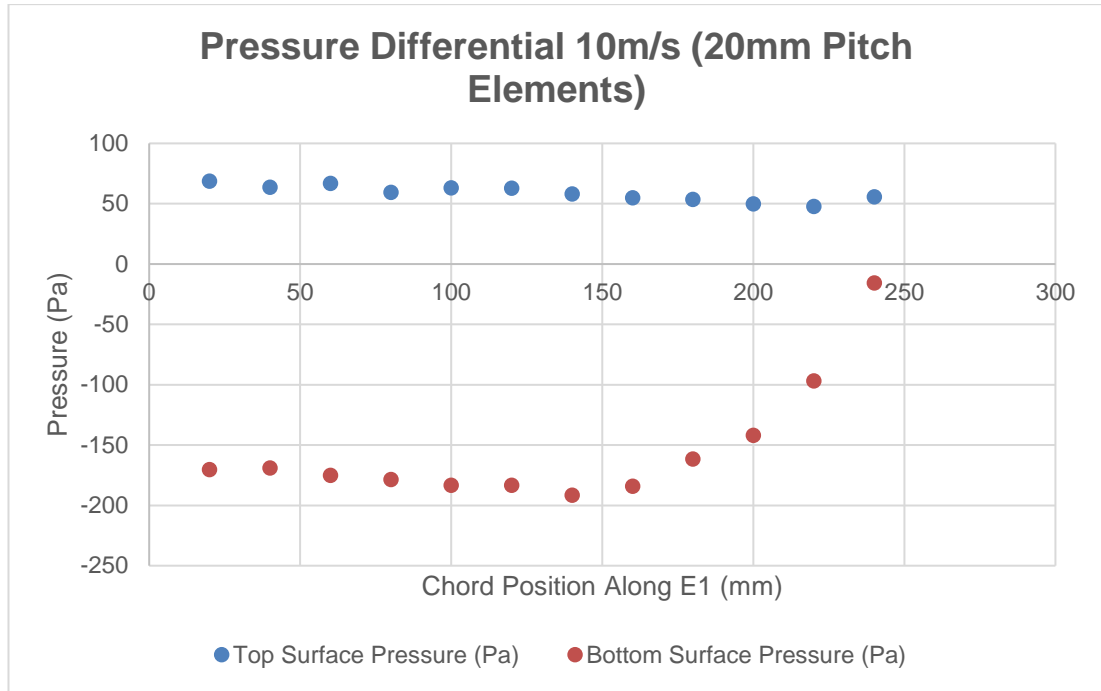
Figure 19 - 20 mm pitch element Aerostrip measurement of pressure distribution acting on E1 at 15 m/s freestream velocity.

Using the same pressure differential methodology and scaling, the total downforce generated at 15 m/s was calculated as 95.073 N.

$$F_D = \sum F_{local} \cdot \frac{950}{25} = \mathbf{95.073\ N}$$

The significant rise in downforce with increased velocity demonstrates the quadratic relationship between velocity and aerodynamic force, as expected from fundamental aerodynamic principles.

4.1.2   8 mm Pitch Sensors

4.1.2.1   Methods

The 8mm pitch configuration was implemented to capture high-resolution surface pressure measurements near the leading edge of E1. With more closely spaced sensing elements than the 20 mm configuration, this setup enables detailed observation of localised pressure peaks, rapid pressure changes, and early boundary layer development.

This higher spatial resolution provides more precise insight into the nature of flow attachment and separation near the front of the aerofoil, which is particularly sensitive to variations in the angle of attack and surface curvature. Smaller pitch configuration improved the ability to detect fine-scale aerodynamic features, particularly in regions where pressure gradients are steepest.

4.1.2.2   10 m/s Freestream Velocity Results

At a freestream velocity of 10 m/s, the 8 mm pitch sensors detected a distinct drop in surface pressure at the leading edge as the airflow is directed towards the lower surface.

This pressure minimum reflects the high acceleration of airflow over the curved geometry at the front of the wing, where flow splits and accelerates beneath the profile as expected.
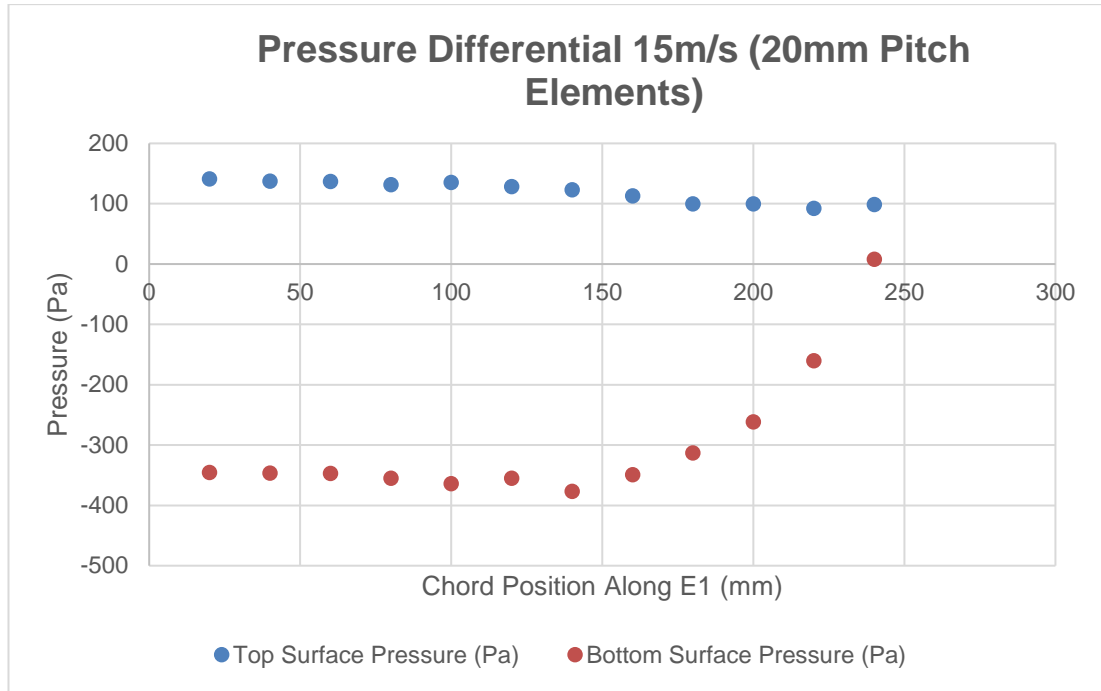

Figure 20 - 8 mm pitch element Aerostrip measurement of pressure distribution acting on E1 at 10 m/s freestream velocity.

As flow progressed along the lower surface of the chord, a gradual increase in pressure was observed, indicating recovery as the flow decelerates toward the trailing edge of E1. The fine resolution of the sensors enabled more precise identification of the pressure peak and the associated pressure gradient.

4.1.2.3   15 m/s Freestream Velocity Results

At a higher freestream velocity of 15 m/s, the pressure distribution follows a similar trend to that observed at 10 m/s but with an increased magnitude across both surfaces. The leading edge pressure drop on the lower surface became more pronounced, indicating stronger flow acceleration.
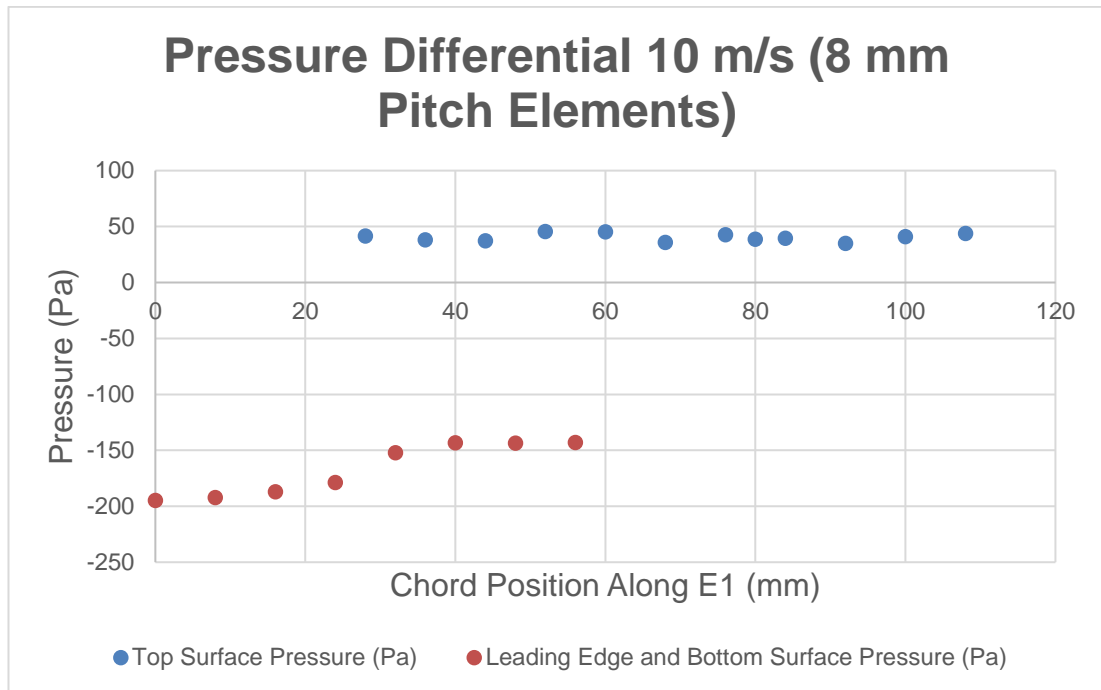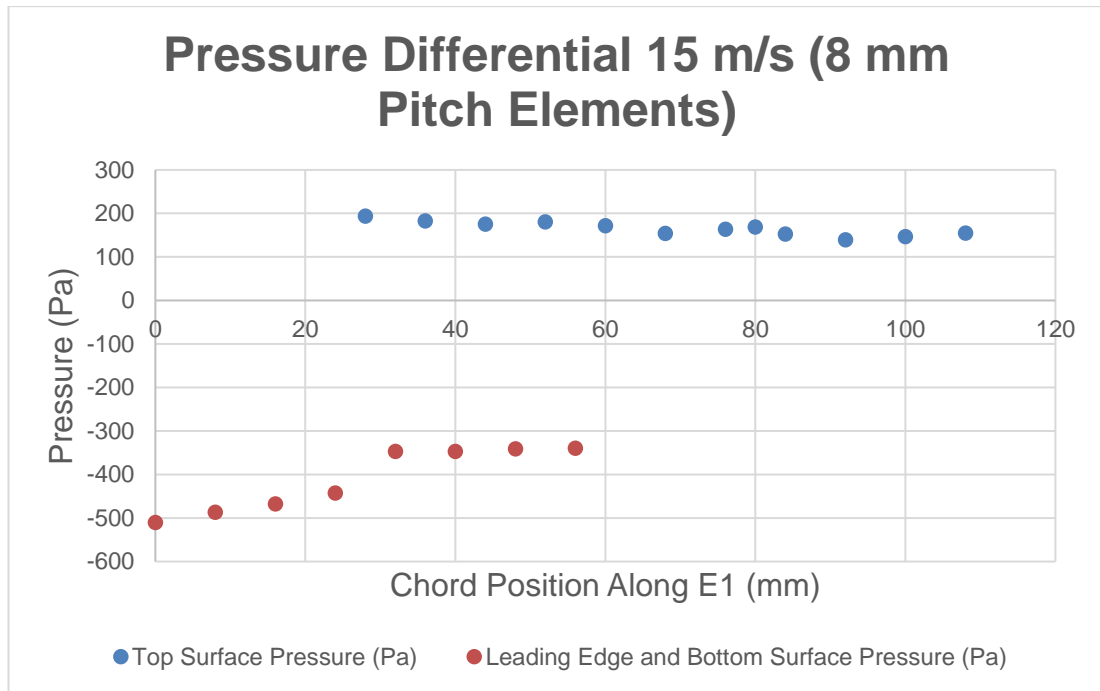
Figure 21 - 8 mm pitch element Aerostrip measurement of pressure distribution acting on E1 at 15 m/s freestream velocity.

Pressure recovery along the chord is more pronounced at higher freestream velocities, with a steeper pressure gradient observed from the leading edge to the mid-chord region on the lower surface. These results reflect an increase in aerodynamic loading and align with theoretical expectations of downforce scaling. The 8 mm pitch resolution also enabled the collection of more accurate local pressure peaks and gradients than the coarser 20 mm pitch configuration.

4.2 CFD Simulations

4.2.1 Turbulence Model Setup Methods

To investigate the influence of turbulence modelling on simulation accuracy, three Reynolds-averaged Navier-Stokes (RANS) turbulence models were individually tested in Siemens STAR-CCM+. The three models applied were:

- k-ω SST
- Spalart-Allmaras
- k-ε

Each turbulence model was simulated at Reynolds numbers corresponding to free-stream velocities of 10 m/s and 15 m/s, matching the wind tunnel conditions as described. Simulations were conducted at each configuration, resulting in six individual datasets. Identical mesh and boundary conditions were applied across all models to ensure consistency throughout. Each simulation was activated independently within the RANS framework.

Initial tests using the k-ω SST model served as the baseline configuration due to its proven effectiveness in capturing boundary layer separation and adverse pressure

35

gradients (Section 2.7.6). The Spalart-Allmaras model was selected to evaluate its performance in near-wall flow conditions with lower computational cost, while the standard k-ε model was included to assess its suitability in free-shear flow environments despite its known limitations in predicting near-wall separation.

Simulation outputs extracted surface pressure distribution along the upper and lower surfaces of the rear wing, specifically at chordwise positions of E1, matching Aerostrip sensor locations. This allowed for direct comparison with experimental pressure data and evaluation of each model's prediction accuracy.

4.2.2   10 m/s Freestream Velocity Results

The predicted surface pressure distributions along the chord's upper and lower surfaces of the rear wing assembly using three turbulence models in separate simulations: k-ω SST, k-ε and Spalart-Allmaras are presented. Each test was conducted at a Reynolds number of 3.35 x 10^5, equivalent to a freestream wind velocity of 10 m/s.
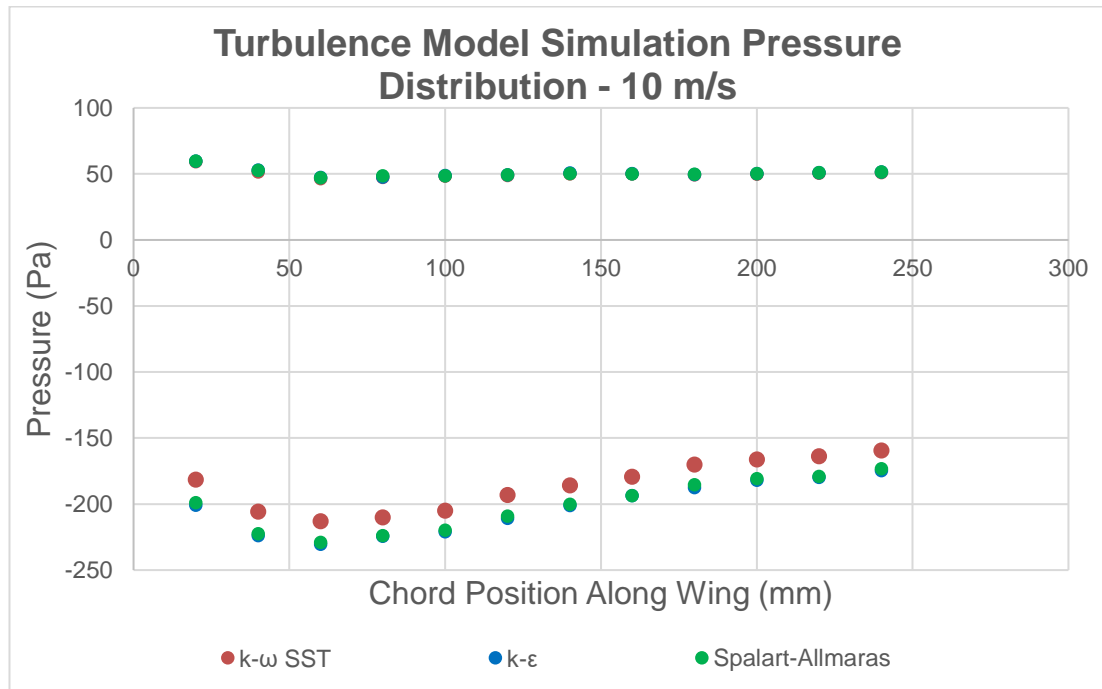
Figure 22 - Turbulence Model Simulation Pressure Distribution Data Prediction at 10 m/s Velocity.

All three models show similar general trends across both the upper and lower surfaces. The upper surface pressure distribution remains relatively consistent between models. The variation is minimal and consistent along the high-pressure region. On the lower surface, a more pronounced pressure drop is observed at the leading edge, with clear variation between models. The k-ω SST model shows a higher pressure distribution compared to the other two models along the lower surface.

4.2.3 15 m/s Freestream Velocity Results

Predicted surface pressure distributions along the chord's upper and lower surfaces of the rear wing model using three turbulence models: k-ω SST, k-ε and Spalart-Allmaras is shown. All simulations were conducted at a free-stream velocity of 15 m/s, corresponding to a Reynolds number of 5.03×10^5, consistent with the higher wind tunnel test condition.
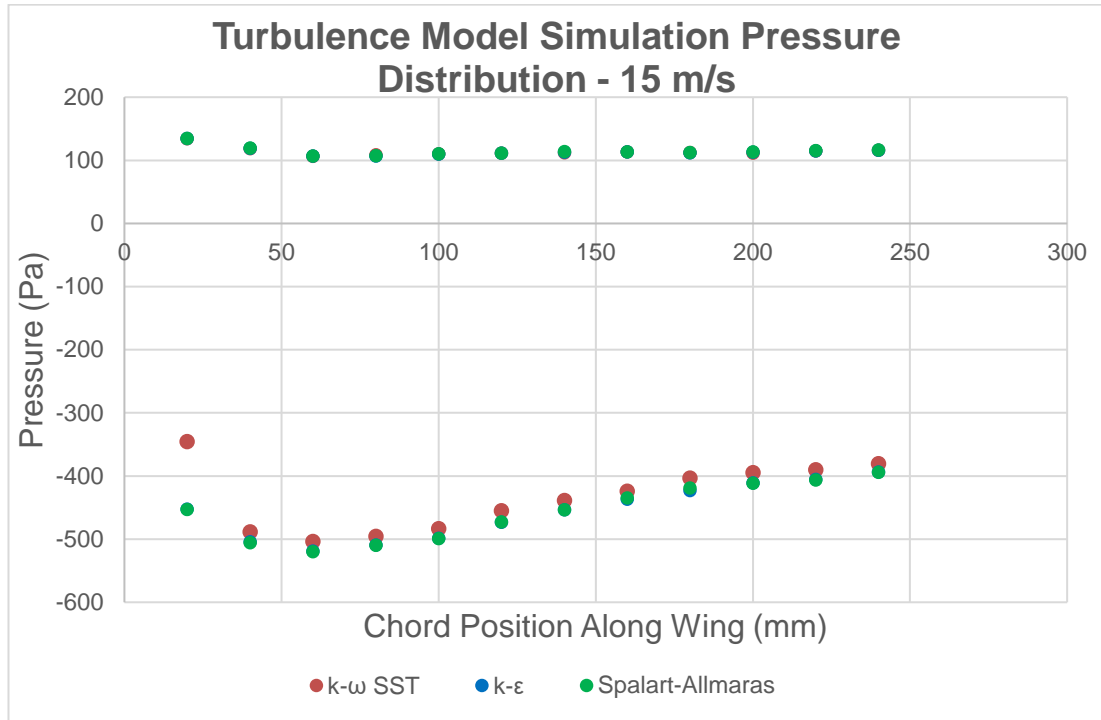
Figure 23 – Turbulence Model Simulation Pressure Distribution Data Prediction at 15 m/s Velocity.

As expected, the increased freestream velocity leads to a more significant pressure differential across the wing. Compared to the 10 m/s case, the pressure gradient at 15 m/s is steeper, especially near the leading edge of the lower surface.

While the general shape of the pressure distribution remains consistent, variations are observed in the magnitude of pressure peaks. The k-ω SST model predicts a higher leading edge pressure peak before dropping closer to alternate model predictions further downstream.

These results establish a baseline for comparing turbulence model performance under matched Reynolds number conditions. The extracted pressure data will be directly compared with wind tunnel measurements to evaluate the predictive accuracy of each turbulence model.

5 Analysis

5.1 Turbulence Model Validation

To evaluate simulation accuracy, surface pressure predictions from three RANS turbulence models, k-ω SST, k-ε and Spalart-Allmaras, are compared with Aerostrip experimental wind tunnel measurements at both 10 m/s and 15 m/s free-stream velocities. This comparison assesses each model's ability to replicate pressure distribution trends along the chord of the rear wing.

At both wind speeds, all three turbulence models produced nearly identical pressure distributions on the upper surface, showing consistent predictive performance in regions of steady flow. This observation supports findings from Zhang et al. [26], who showed that RANS models typically perform well in stable flow.

However, distinct variations are observed along the chord of the lower surface, where flow accelerates significantly near the leading edge and produces steep pressure gradients. In this region, the k-ω SST model predicted slightly higher pressure magnitudes compared to Spalart-Allmaras and k-ε models. This suggests that the k-ω SST model more effectively predicts flow acceleration and boundary layer interactions on the lower surface.

Figure 24 – Turbulence Model Simulation Pressure Distribution Data Prediction at 10 m/s Velocity compared to Aerostrip Measurement Data.

At 10 m/s, the experimental data shows a slightly higher pressure on the upper surface than predicted by all turbulence models. This discrepancy can be introduced from limitations in turbulence models that approximate flow stability and wall-normal pressure gradients. RANS models may underpredict pressure retention, especially in areas with viscous effects; however, finding the balance between computational

38

efficiency and prediction accuracy is essential in a heavily restricted testing environment (Section 2.9).
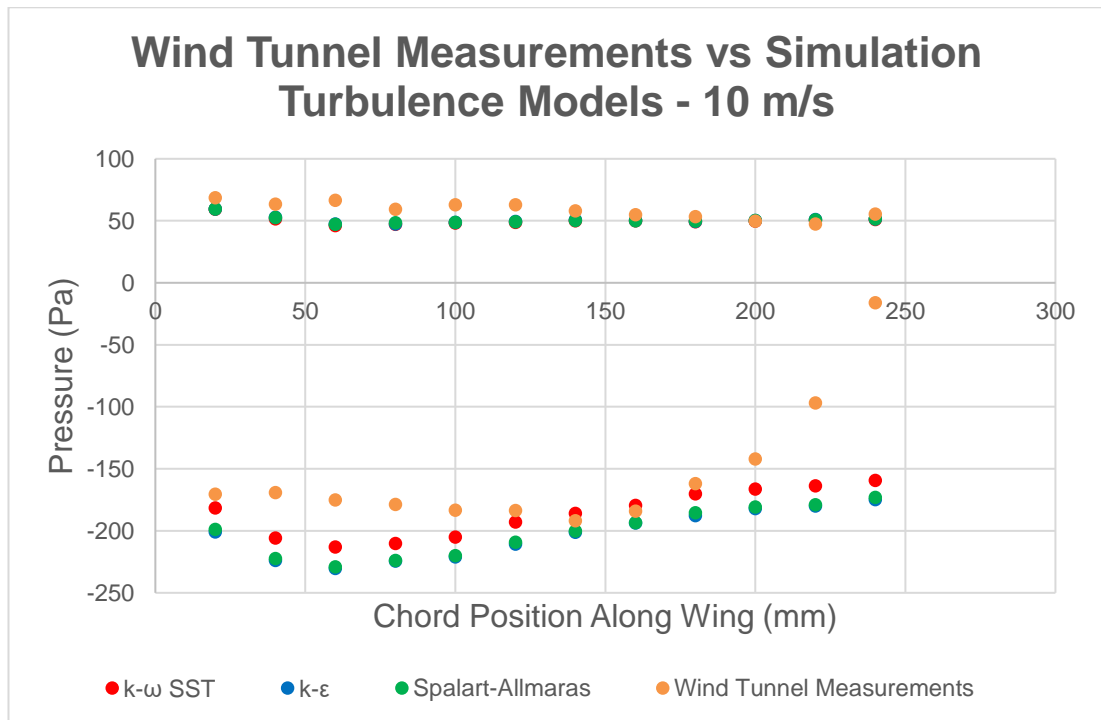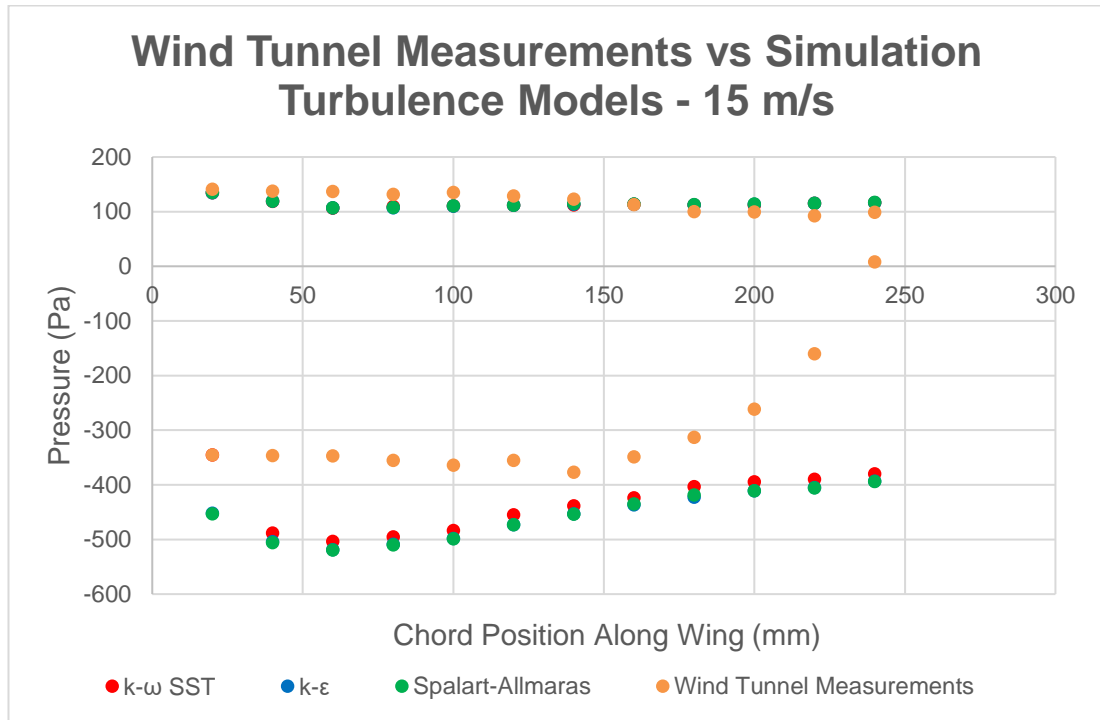

Figure 25 - Turbulence Model Simulation Pressure Distribution Data Prediction at 10 m/s Velocity compared to Aerostrip Measurement Data.

At 15 m/s, the leading edge pressure value on the lower surface aligns almost identically with the k-ω SST prediction, while Spalart-Allmaras and k-ε models are shown to overestimate the pressure drop. This suggests that these models inaccurately simulate how the flow splits at the leading edge. Additionally, the k-ω SST model shows closer alignment with wind tunnel measurement data along the lower surface chord overall compared to other models.

The k-ω SST turbulence model will be used as the reference model in subsequent comparisons with wind tunnel results. This validation highlights the importance of selecting an appropriate turbulence model, particularly when utilising simulation outputs for real-world aerodynamic development. In motorsport, where marginal gain can lead to great success, subtle variations between models can significantly influence design decisions and performance optimisation.

5.2 Large-Scale Aerodynamic Trend Comparison (20 mm Pitch Element Sensors)

Surface pressure distributions are measured along the chord of a Formula 1-style rear wing using Aerostrip sensors, specifically on the upper and lower surfaces of E1, using the 20 mm pitch element configuration. CFD simulation predictions use the k-ω SST turbulence model, proven as the closest aligning to measurements. The results are shown for wind tunnel test velocities of 10 m/s and 15 m/s:
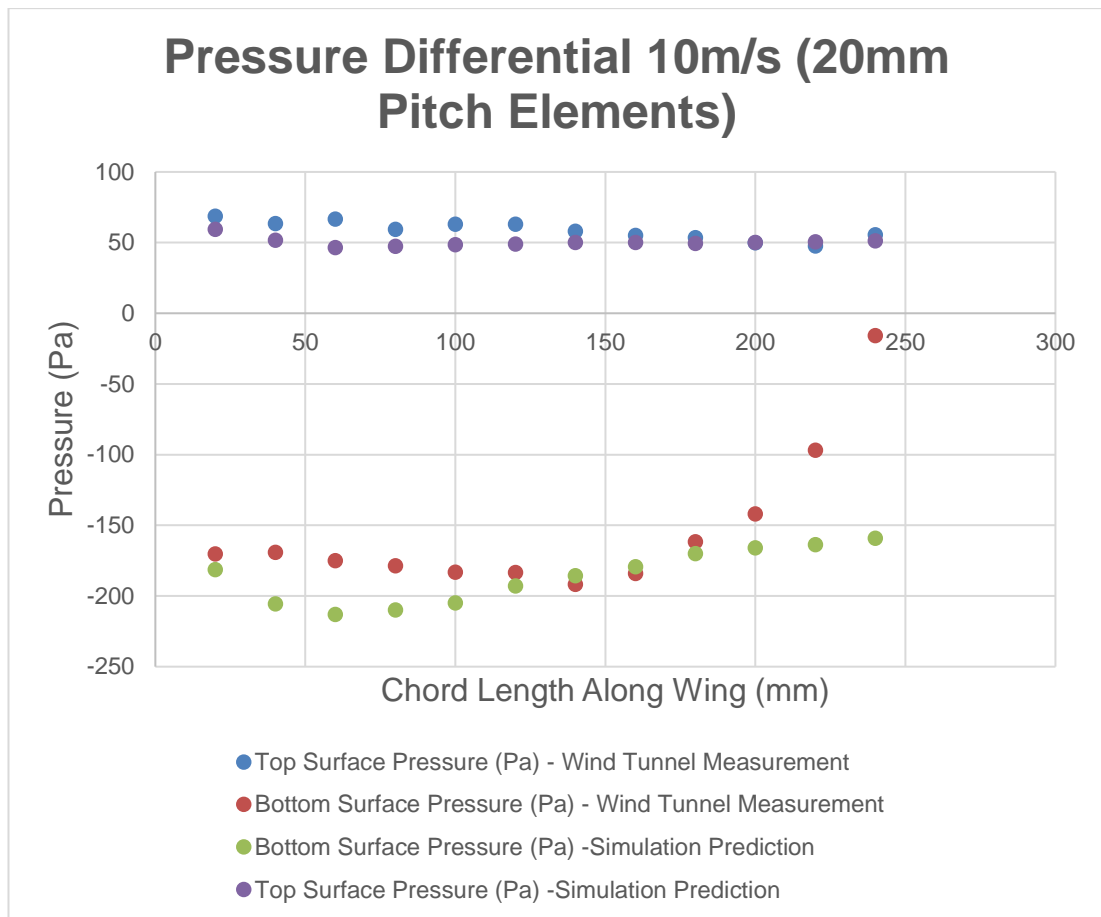
Figure 26 - Comparison of Aerostrip 20 mm pitch element wind tunnel measurements to simulation predictions using k-ω SST turbulence model at Freestream Velocity of 10 m/s.
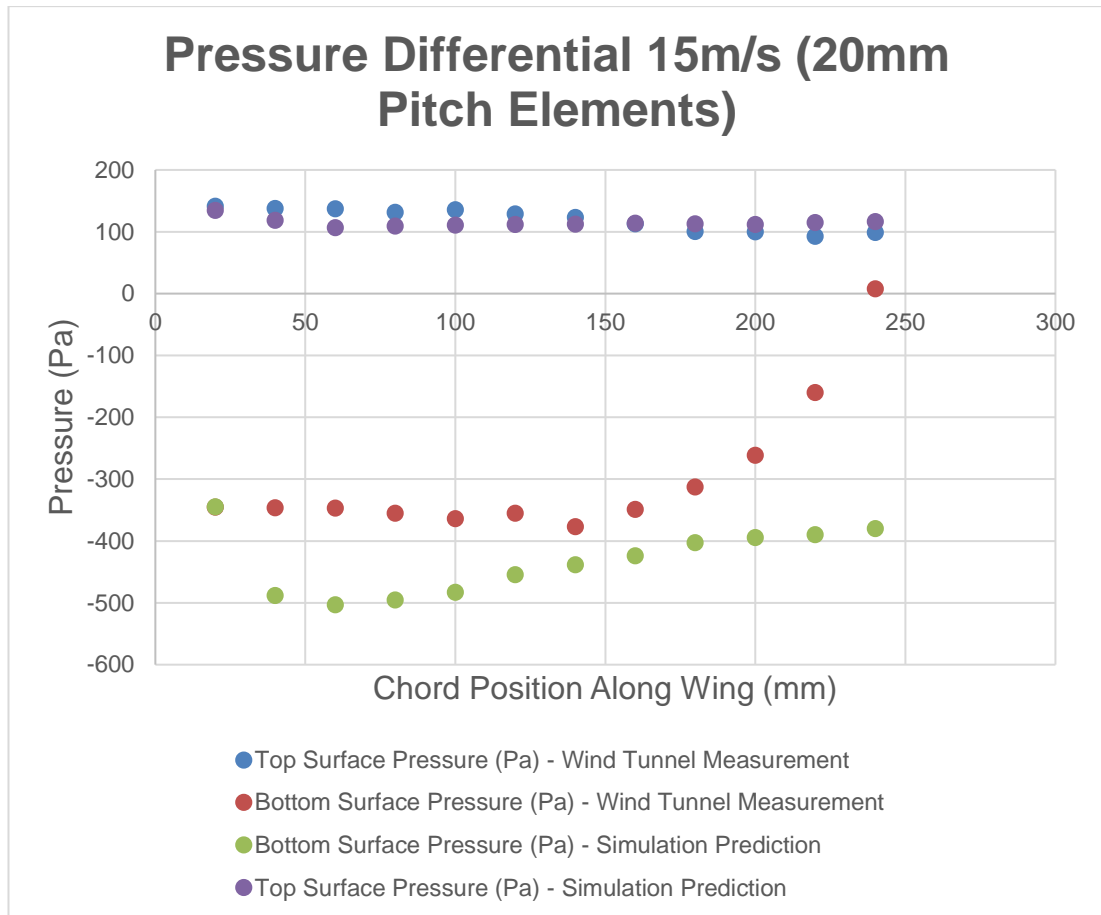
Figure 27 - Comparison of Aerostrip 20 mm pitch element wind tunnel measurements to simulation predictions using k-ω SST turbulence model at Freestream Velocity of 15 m/s.

At both velocities, the general pressure distribution follows the expected aerodynamic trend, with the lower surface experiencing a pressure drop due to the increased airflow velocity. In contrast, the upper surface maintains relatively high pressure. This pressure differential generates downforce acting on the wing, in line with the aerodynamic principles described in Sections 2.4 and 2.5.

It was observed that a clear divergence between experimental and simulated pressure values is evident on the lower surface. Approximately 200 mm along the chord, while simulated predictions continue to follow the curvature of the aerofoil, the wind tunnel data shows a rapid increase in pressure, approaching ambient conditions. This sharp change strongly suggests boundary layer flow separation, which detaches from the surface due to an adverse pressure gradient, as discussed in Section 2.6.2.

This separation effect is evident at both 10 m/s and 15 m/s, indicating consistency in the physical behaviour and proving the consistency of the Aerostrip sensors. Additionally, the location of separation remains at approximately the same chord region across both speeds, suggesting that the flow transition and boundary layer detachment are largely insensitive to the moderate increase in Reynolds number within the test range. This reinforces the validity of Reynolds number scaling, as discussed in Section 2.7.5.

The downforce values computed from the experimental Aerostrip data and CFD simulations also reflect this behaviour.

- At 10 m/s, the measured downforce is 48.562 N, while CFD predicted 53.871 N, yielding a 10.4% error.
- At 15 m/s, the experimental result is 95.073 N, whereas the simulation predicted 124.890 N, resulting in a more significant 27.1% error.

The increasing discrepancy at higher velocity may be due to the limitations of RANS-based turbulence modelling in predicting separated, unsteady flow regions, as highlighted in Section 2.7.6.

This trend reflects Newton's Third Law, as the increased downward deflection of fast-moving air results in a greater aerodynamic reaction force at higher speeds. However, it also illustrates the challenge of accurately modelling complex viscous and turbulent effects numerically, particularly in real-world geometries.

To evaluate pressure distribution across the wingspan, Aerostrip sensors are installed at both quarter-span locations on each surface of E1 during select tests.

- At 10 m/s, the upper surface pressure varied by only 2.81%, while the lower surface showed a 13.49% variation.
- Similarly, at 15 m/s, upper surface variation is 1.30% and lower surface variation is 13.42%.

The more significant inconsistency on the bottom surface may be caused by real-world asymmetries in the test setup, including slight misalignments during mounting, interference from the central beam and bracket, or minor inaccuracies in the physical wing geometry itself. Subtle variations in wing curvature, thickness or surface material can cause local changes in flow behaviour, making the lower surface increasingly susceptible to inaccurate pressure readings. In contrast, the upper surface showed stronger symmetry, indicating that these factors had a lesser influence on the flow above the wing.

Overall, the findings demonstrate that the 20 mm pitch Aerostrip configuration effectively captures large-scale aerodynamic trends, including pressure gradients and regions of flow separation. The results provide a valuable validation baseline against CFD predictions, reinforcing the sensor's ability to capture real-world aerodynamic effects in motorsport conditions.

The data aligns with expected aerodynamic trends and behaviour, with the lower surface experiencing more negative pressure (stronger suction) than the positive pressure on the upper, a typical characteristic of effective downforce-generating wings. However, there is evident variation between the wind tunnel-measured surface pressure values and the simulated predictions, which is due to real-world aerodynamic factors contributing to increased flow separation, boundary layer detachment,

turbulent wake structures and viscous effects. The boundary layer lost momentum and detached from the surface.

5.3 Fine-Scale Pressure Peak Comparison (8 mm Pitch Element Sensors)

High-resolution surface pressure measurements from the leading edge of E1 were measured using the 8 mm pitch Aerostrip sensor strips at freestream velocities of 10 m/s and 15 m/s. These are directly comparable to CFD predictions using the k-ω SST turbulence model.

At both speeds, the finer pitch configuration provides distinct aerodynamic features that are less clearly resolved by the 20 mm pitch sensors. The increased resolution offers a closer insight into rapid pressure changes near the leading edge, particularly where the airflow first hits the curved geometry of the wing and splits between the upper and lower surfaces.

Figure 28 - Comparison of Aerostrip 8 mm pitch element wind tunnel measurements to simulation predictions using k-ω SST turbulence model at Freestream Velocity of 10 m/s.

At 10 m/s, a sharp pressure drop is observed on the lower surface immediately at the leading edge. This minimum pressure region reflects the acceleration of flow beneath the aerofoil, consistent with Bernoulli's principle. It is observed that the pressure drop in the experimental data is slightly lower and more abrupt than in the simulation results. This suggests that the flow begins to split and accelerate sooner than predicted,

43

likely due to the differences in the simulated mesh refinement or idealised assumptions about the inlet conditions and surface curvature.

In contrast, the upper surface shows good agreement between the wind tunnel and simulation data, with no indication of flow separation. Pressure remains relatively stable across the measured chord length, which emphasises attached flow and reinforces the effectiveness of the k-ω SST turbulence model in predicting pressure retention in these regions.

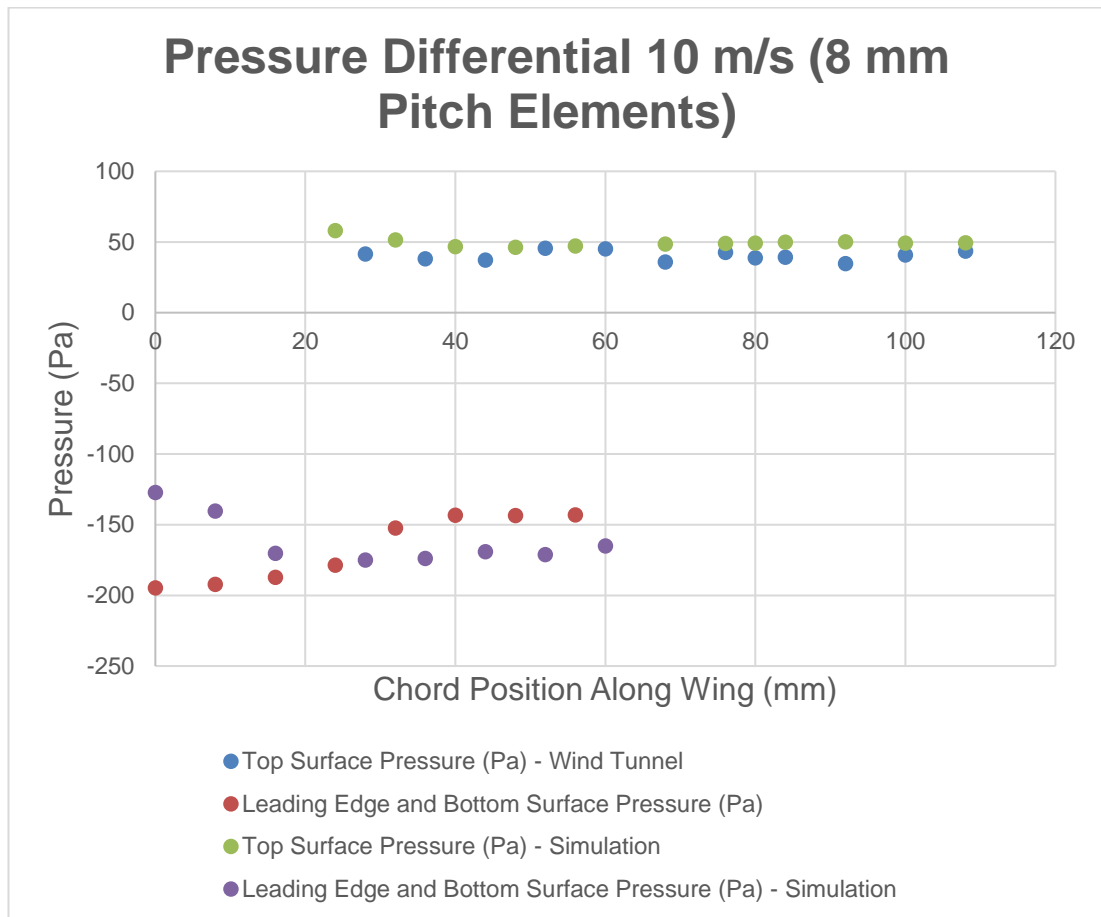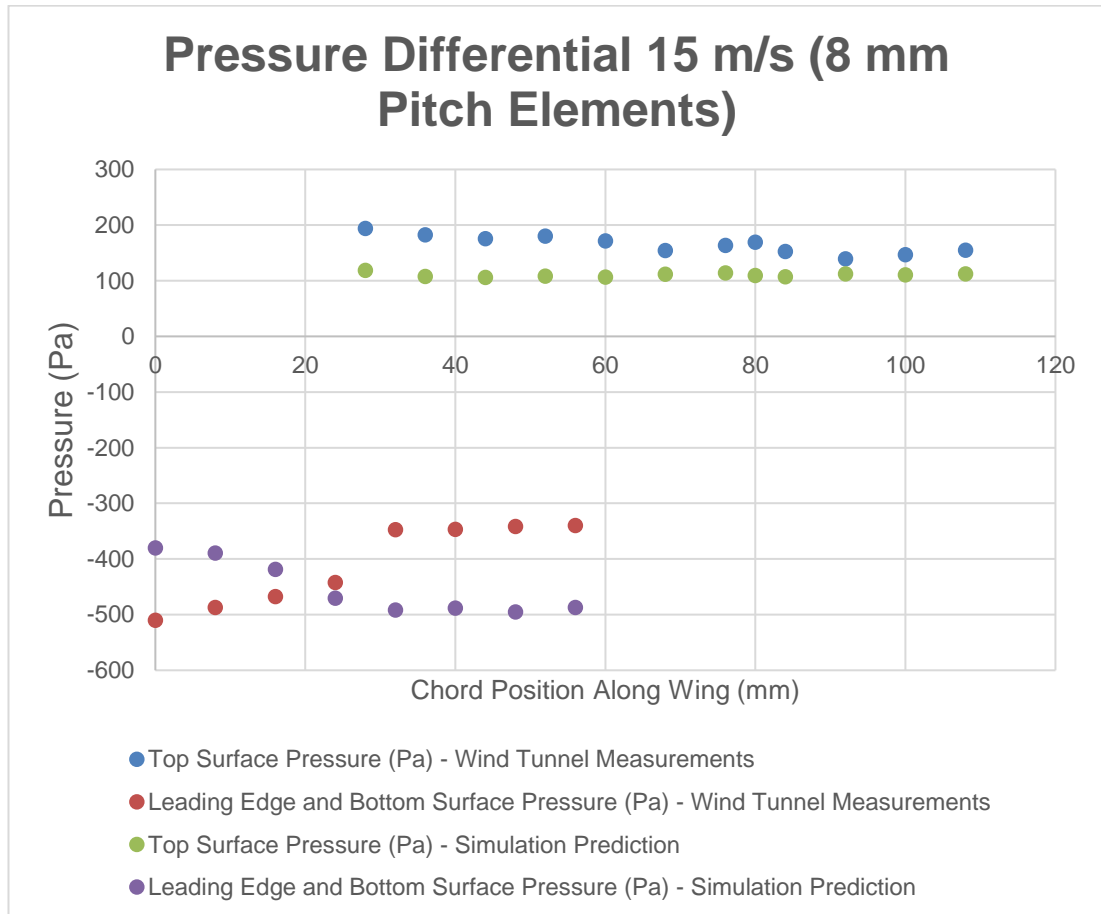*Figure 29 - Comparison of Aerostrip 8 mm pitch element wind tunnel measurements to simulation predictions using k-ω SST turbulence model at Freestream Velocity of 15 m/s.*

At 15 m/s, the magnitude of pressure on the upper surface indicates that the simulation results are underpredicting along the wing's chord. This discrepancy may be due to the increased velocity gradient at higher freestream speeds, amplifying the effect of boundary layer behaviour on surface pressure. The simulation may be underestimating the wall-normal pressure recovery due to limitations in turbulence modelling, mesh density near the wall or boundary condition assumptions.

Another contributing factor could be sensor boundary proximity. At higher speeds, minor inaccuracies in the physical wing surface or leading edge may influence the local pressure distribution more strongly, especially if the simulation assumes a perfectly smooth profile.

At this wind velocity, the Aerostrip measured pressure drop becomes more pronounced and abrupt on the lower surface, occurring earlier in the chord than predicted by CFD simulations. This further supports the idea that the simulation may underestimate flow acceleration or delay leading edge behaviour. These findings align with the limitations of RANS models in capturing steep gradients and initial boundary layer transitions.

During both tests, no evidence of boundary layer separation is detected on either surface. Pressure distributions follow the expected trends, with strong agreement across both wind speeds, suggesting that the boundary layer remains attached in the observed chord region. This is expected, as the 8 mm sensor only covers the front portion of the wing's chord where the pressure gradient does not cause separation. This consistency supports the reliability of the Aerostrip sensor, in agreement with validation by Zhang et al. [1] and Subramanian et al. [2].

These results also confirm accurate Reynolds number scaling between the 10 m/s and 15 m/s conditions. Although the magnitude of pressure changes with velocity (as expected from dynamic pressure scaling), the overall shape and distribution remain consistent, validating the assumptions described in Section 2.7.5.

Overall, the high-resolution measurements from the 8 mm pitch Aerostrip reveal aerodynamic behaviour that would be difficult to detect with coarse instrumentation. The leading edge pressure drop and recovery are resolved with clarity, providing strong support for Aerostrip's ability to detect critical flow features in the boundary layer.

5.4   Combined Sensor Elements

To evaluate the consistency of Aerostrip measurements across varying resolutions, data from both the 20 mm and 8 mm pitch configurations are plotted together for each freestream velocity. This allowed for a direct visual comparison of pressure trends along the chord of the wing.
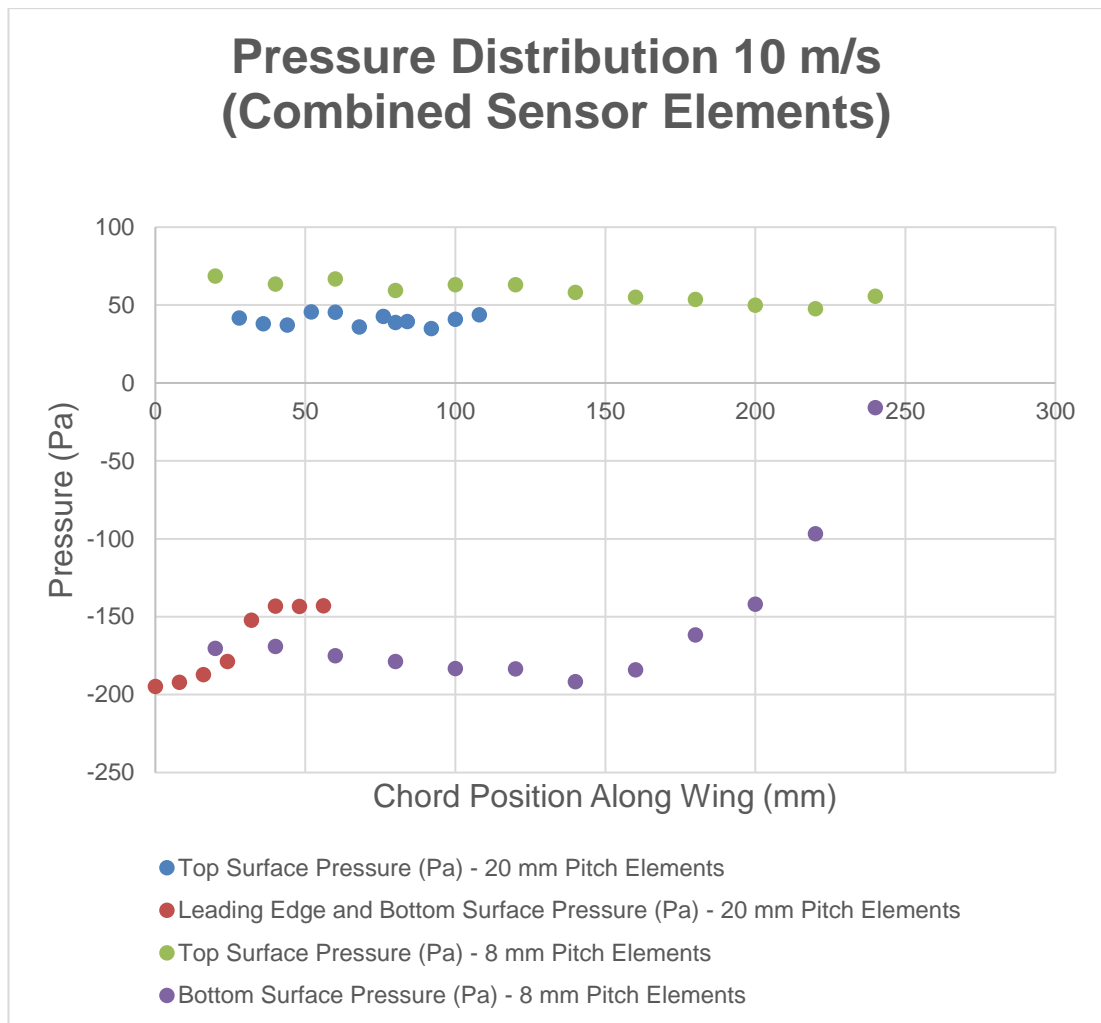
Figure 30 - Combined Aerostrip Sensor Measurements from both 20- and 8-mm pitch elements at 10 m/s freestream velocity.
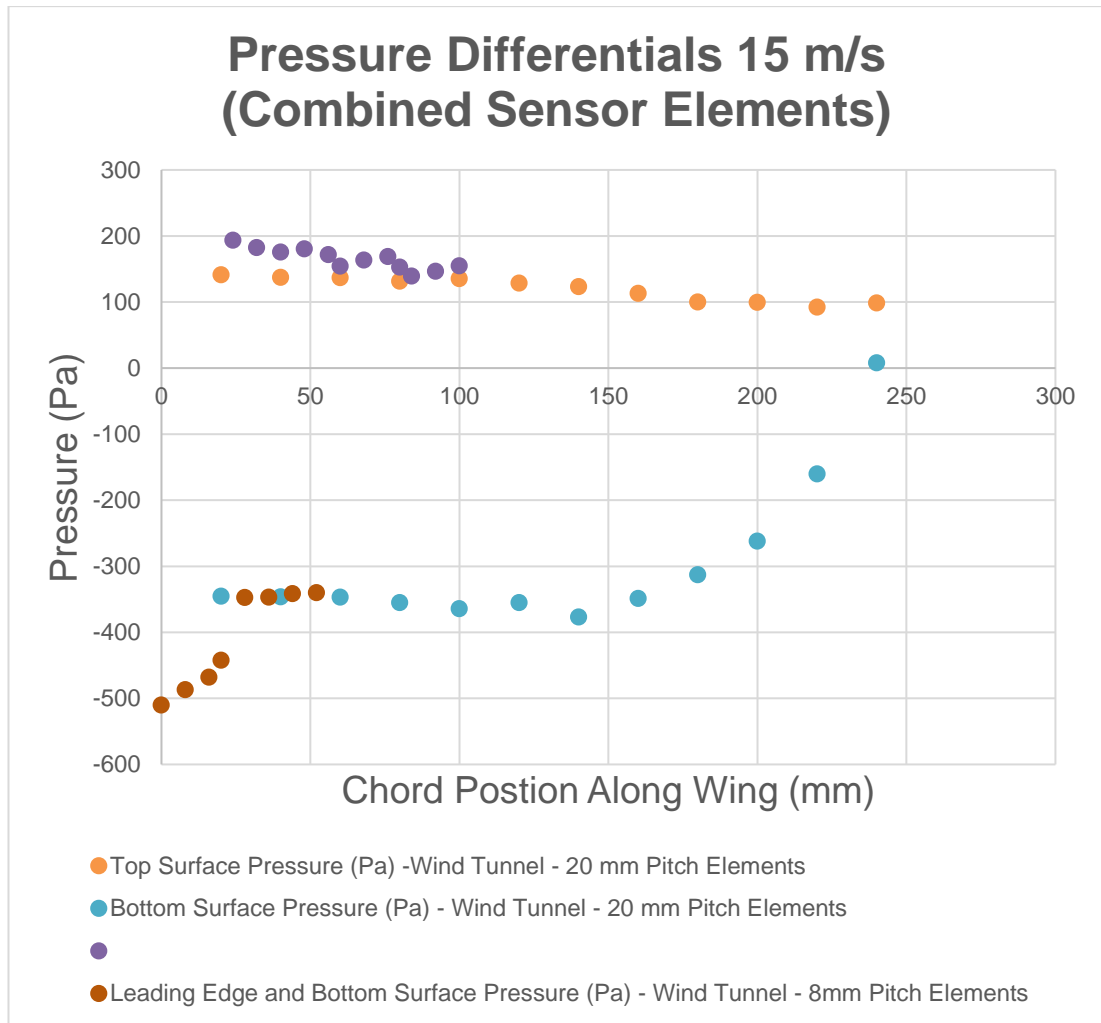
Figure 31 - Combined Aerostrip Sensor Measurements from both 20- and 8-mm pitch elements at 15 m/s freestream velocity.

At both 10 and 15 m/s, the combined datasets show strong agreement in overlapping regions, with few discontinuities or unexpected offsets between the two sensor types. The 8 mm pitch elements captured finer detail in the leading edge region, whereas the 20 mm pitch elements exhibited a larger-scale pressure trend along the remainder of the chord. The smooth transition between the two datasets reinforces the accuracy and repeatability of the Aerostrip sensors under consistent test conditions.

Although data for each pitch is collected in separate runs, which can cause variance in results, the close alignment across multiple tests shows minimal variability in the open-loop wind tunnel conditions. It confirms that the recorded pressure distributions are reliable. This supports the integration of fine- and coarse-resolution data for more detailed aerodynamic analysis without excessively compromising accuracy.

6 Aerodynamic Evaluation & Future Development

6.1 Discussion

The Aerostrip's ability to capture high-resolution pressure gradients, especially the 8 mm pitch configuration, enabled the detection of leading edge flow acceleration and pressure recovery, thereby reinforcing the sensor's value as an aerodynamic measurement tool. Notable pressure discrepancies, especially in the lower surface boundary layer, are associated with real-world flow separation and wake turbulence. These effects are difficult to predict using RANS-based turbulence models.

Although only partial chord coverage was achieved due to concerns that overlapping sensors would introduce flow disturbances, the collected data is sufficient to identify key aerodynamic behaviours and allowed for downforce comparison. The decision to limit chord coverage was necessary to preserve the validity of pressure measurement data and minimise airflow disruption.

Importantly, this study marks the first experimental validation of USM's simulation predictions for airflow behaviour and component performance. This highlights the Aerostrip's role in enhancing confidence in the team's existing CFD workflow by utilising a non-invasive testing method that is reusable and non-destructive to component materials, thereby making it an effective alternative to traditional testing methods such as pressure taps or pressure-sensitive paint. The observed flow separation in measured outputs provides direct evidence for evaluating the aerodynamic wing model and adjusting parameters, such as the angle of attack, which is currently fixed in the wing design.

6.2 Future Work

Improvements can be made in future testing to enhance data quality and further extend analysis. One key development would be to lengthen the chordwise coverage of the Aerostrip sensor. Installing an additional Aerostrip to measure the full chord length would provide a comprehensive understanding of pressure recovery and boundary layer detachment in the trailing edge region. However, careful attention would be needed to optimise mounting methods that minimise airflow interference while maintaining high data accuracy.

Further improvements could be made to the structural rigidity of the custom-designed mounting system. During testing, the aluminium mounting plate showed minor oscillations and flexing under load, which may have introduced variability into the pressure measurements. Replacing the plate with a stiffer material or reinforcing the structure would improve measurement stability and overall test repeatability.

The feasibility of on-track testing should be explored to expand the applicability of the Aerostrip system. However, one limitation of live data collection is the requirement for a wired connection to operate Chameleon software, restricting testing to static environments or the use of passenger vehicles. Future development of the Aerostrip

system could incorporate wireless data acquisition, onboard storage, or battery-powered logging to support dynamic tests for single-seater race cars.

In terms of aerodynamic optimisation, the observed boundary layer separation at the mid-chord region suggests that refinement to USM's rear wing design will be beneficial. Altering the angle of attack of the main element as it connects to the body of the race car could delay separation and improve aerodynamic efficiency. Additionally, modifying endplate geometry may help to control vortex formation and improve spanwise pressure uniformity.

Repeating identical tests with refined geometries in the rear wing design would provide valuable comparative data to show future improvements to airflow management using the Aerostrip sensor strip technology. This data serves as a baseline for the ongoing development of the USM race car and validation of CFD simulations using updated parameters.

Given the numerous restrictions imposed by the FIA on wind tunnel testing time and CFD simulation hours, the Aerostrip's low cost, reusability and ease of implementation make it a valuable tool for modern aerodynamic development in motorsport.

7 Conclusions

This study successfully demonstrates the application of Pressure Profile System's Aerostrip for aerodynamic development in motorsport. By implementing Aerostrip sensors onto the element of a Formula 1-style rear wing and testing in controlled wind tunnel conditions, detailed surface pressure distributions are measured. Real-world aerodynamic effects, such as flow separation, boundary layer development and viscous flow, are analysed to understand the difference between theoretical predictions and actual aerodynamic behaviour.

To validate the findings, an identical model assembly was created and simulated in CFD using Siemens STAR-CCM+ and a range of RANS turbulence models are tested. These simulations enabled a direct comparison of predicted and measured pressure distributions at two Reynolds number conditions. The k-ω SST turbulence model provided the closest agreement with experimental results, particularly in regions near the leading edge of the aerofoil with steep pressure gradients. The variation in predicted downforce values highlights limitations in RANS-based turbulence models and suggests that real-world aerodynamic effects, such as boundary layer separation and spanwise pressure variation, must be accounted for during simulation calibration. This analysis highlighted the importance of selecting appropriate turbulence modelling for accurate prediction of flow behaviour.

Differing Aerostrip sensor configurations, with a coarse 20 mm and a finer 8 mm pitch, allowed for the evaluation of large-scale aerodynamic trends as well as fine-scale pressure peaks. Utilising both configurations proved effective in detecting flow acceleration, pressure recovery and potential boundary layer separation, particularly near the mid-chord of the element's lower surface.

The Aerostrip measured data reinforced key aerodynamic principles. Pressure differentials aligned with Bernoulli's Principle, demonstrating how changing velocity influences pressure distribution, while the generation of downforce validated Newton's Third Law through the equal and opposite reaction of airflow deflection. Additionally, the evident mid-chord separation showed the importance of minimising the transition from laminar to turbulent flow for optimal aerodynamic efficiency.

Overall, the Aerostrip sensor system has proven to be a reusable, accurate and flexible tool for aerodynamic testing in motorsport. Its non-intrusive design and compatibility with CFD make it well-suited in an environment with many limitations in wind tunnel and simulation resources. With further development in sensor coverage and hardware reduction, the Aerostrip is a highly promising newcomer for enhancing real-world aerodynamic validation and vehicle performance optimisation in future motorsport applications.

References

[1]   D. Zhang, S. Subramanian, R. Hampson, W. Jackson, K. Kontis, G. Dobie and C. Macleod, 'Automotive Aerodynamics Sensing Using Low-Profile Pressure Sensor Strip', *IEEE Trans Instrum Meas*, vol. 72, 2023, doi: 10.1109/TIM.2023.3292963.

[2]   S. Subramanian, R. Hampson, D. Zhang, K. Kontis, G. Dobie, C. Macleod and J. Son, 'Characterization of a Low Profile, Rapidly Deployable, MEMS Pressure Sensor Array for Aerodynamic Applications', in *AIAA Science and Technology Forum and Exposition, AIAA SciTech Forum 2022*, American Institute of Aeronautics and Astronautics Inc, AIAA, 2022. doi: 10.2514/6.2022-0305.

[3]   D. Martins, J. Correia, and A. Silva, 'The influence of front wing pressure distribution on wheel wake aerodynamics of a f1 car', *Energies (Basel)*, vol. 14, no. 15, Aug. 2021, doi: 10.3390/en14154421.

[4]   W. Li, T. Liu, P. Martinez-Vazquez, Z. Chen, X. Huo, D. Liu and Y. Xia, 'Correlation tests on train aerodynamics between multiple wind tunnels', *Journal of Wind Engineering and Industrial Aerodynamics*, vol. 229, Oct. 2022, doi: 10.1016/j.jweia.2022.105137.

[5]   B. G. McLachlan and J. H. Bell, 'Pressure-sensitive paint in aerodynamic testing', *Exp Therm Fluid Sci*, vol. 10, no. 4, pp. 470–485, May 1995, doi: 10.1016/0894-1777(94)00123-P.

[6]   J. L. Aider, L. Elena, Y. Le Sant, F. Bouvier, M. C. Merienne, and J. L. Peron, 'Pressure-sensitive paint for automotive aerodynamics', in *SAE Technical Papers*, SAE International, 2001. doi: 10.4271/2001-01-0627.

[7]   J. Katz, 'Aerodynamics of Race Cars', pp. 28–30, 2025, doi: 10.1146/annurev.fluid.

[8]   tec-science, 'Flow separation (boundary layer separation)'. Accessed: Oct. 24, 2024. [Online]. Available: https://www.tec-science.com/mechanics/gases-and-liquids/flow-separation-boundary-layer-separation/

[9]   Z. Qiu and H. Zhang, 'Aerodynamics-based design of the rear wing of a sports car', *Applied and Computational Engineering*, vol. 11, no. 1, pp. 310–317, Sep. 2023, doi: 10.54254/2755-2721/11/20230245.

[10]   Max Taylor, 'Aerodynamic Studies of a 2022 F1 Car', Max Taylor – Aerodynamics and Motorsport Engineering. Accessed: Mar. 26, 2025. [Online]. Available: https://maxtayloraero.com/2022/01/17/aerodynamic-studies-of-a-2022-f1-car/

[11] Z. Guo, T. Zhang, F. Zhou, and F. Yu, 'Design and experiments for a kind of capacitive type sensor measuring air flow and pressure differential', *IEEE Access*, vol. 7, pp. 108980–108989, 2019, doi: 10.1109/ACCESS.2019.2933485.

[12] National Aeronautics and Space Administration, 'Bernoulli's Principle', www.nasa.gov. Accessed: Mar. 3, 2025. [Online]. Available: https://www.nasa.gov/wp-content/uploads/2023/06/bernoullis-principle-k-4-02-09-17-508.pdf

[13] David Halliday, Robert Resnick, and Jearl Walker, *Fundamentals of Physics*, 10th Edition. Wiley, 2013.

[14] K. Walters and W. M. Jones, 'Measurement of viscosity', in *Instrumentation Reference Book*, Elsevier, 2003, pp. 45–52. doi: 10.1016/B978-075067123-1/50006-5.

[15] Hermann Schlichting and Klaus Gersten, *Boundary-Layer Theory*, 9th ed. Springer Berlin Heidelberg, 2016. doi: 10.1007/978-3-662-52919-5

[16] G. Leishman, *Introduction to Aerospace Flight Vehicles*. Embry-Riddle Aeronautical University, 2022. doi: 10.15394/eaglepub.2022.1066.

[17] Walter Frei, 'Which Turbulence Model Should I Choose for My CFD Application?'. COSMOL. Accessed: Mar. 19, 2025. [Online]. Available: https://www.comsol.com/blogs/which-turbulence-model-should-choose-cfd-application

[18] tec-science, 'Flow separation (boundary layer separation)'. Accessed: Mar. 25, 2025. [Online]. Available: https://www.tec-science.com/mechanics/gases-and-liquids/flow-separation-boundary-layer-separation/

[19] W. Hucho and G. Sovran, 'Aerodynamics of Road Vehicles', *Annu Rev Fluid Mech*, vol. 25, no. 1, pp. 485–537, Jan. 1993, doi: 10.1146/annurev.fl.25.010193.002413.

[20] M. Kalinowski and M. Szczepanik, 'Aerodynamic shape optimization of racing car front wing', *IOP Conf Ser Mater Sci Eng*, vol. 1037, no. 1, p. 012058, Feb. 2021, doi: 10.1088/1757-899X/1037/1/012058.

[21] J. Wang, H. Li, Y. Liu, T. Liu, and H. Gao, 'Aerodynamic research of a racing car based on wind tunnel test and computational fluid dynamics', *MATEC Web of Conferences*, vol. 153, p. 04011, Feb. 2018, doi: 10.1051/matecconf/201815304011.

[22] V. G. Kirtskhalia, 'Speed of Sound in Atmosphere of the Earth', *Open Journal of Acoustics*, vol. 02, no. 02, pp. 80–85, 2012, doi: 10.4236/oja.2012.22009.

[23] P. M. Sforza, 'Quasi-One-Dimensional Flow Equations', in *Theory of Aerospace Propulsion*, Elsevier, 2012, pp. 35–53. doi: 10.1016/B978-1-85617-912-6.00002-5.

[24] M. H. Zawawi *et al.*, 'A review: Fundamentals of computational fluid dynamics (CFD)', 2018, p. 020252. doi: 10.1063/1.5066893.

[25] G. Łukaszewicz and P. Kalita, *Navier–Stokes Equations*. Cham: Springer International Publishing, 2016. doi: 10.1007/978-3-319-27760-8.

[26] N. Wright and A. Crosato, 'The Hydrodynamics and Morphodynamics of Rivers', in *Treatise on Water Science*, Elsevier, 2011, pp. 135–156. doi: 10.1016/B978-0-444-53199-5.00033-6.

[27] N. Rott, 'Note on the History of the Reynolds Number', *Annu Rev Fluid Mech*, vol. 22, no. 1, pp. 1–12, Jan. 1990, doi: 10.1146/annurev.fl.22.010190.000245.

[28] C. Zhang, C. P. Bounds, L. Foster, and M. Uddin, 'Turbulence modeling effects on the CFD predictions of flow over a detailed full-scale sedan vehicle', *Fluids*, vol. 4, no. 3, Aug. 2019, doi: 10.3390/fluids4030148.

[29] F. R. Menter, 'Two-equation eddy-viscosity turbulence models for engineering applications', *AIAA Journal*, vol. 32, no. 8, pp. 1598–1605, Aug. 1994, doi: 10.2514/3.12149.

[30] Č. Kostić, 'Review of the Spalart-Allmaras turbulence model and its modifications to three-dimensional supersonic configurations', *Scientific Technical Review*, vol. 65, no. 1, pp. 43–49, 2015, doi: 10.5937/STR1501043K.

[31] Federation Internationale de l'Automobile, '2009 FORMULA ONE TECHNICAL REGULATIONS', 2009. Accessed: Mar. 29, 2025. [Online]. Available: https://argent.fia.com/web/fia-public.nsf/7c4f8d883039af6ac125757d00369c58/$file/1-2009_f1_technical_regulations_showing-alterations_17-03-2009.pdf

[32] Federation Internationale de l'Automobile, '2025 FORMULA ONE SPORTING REGULATIONS', 2025. Accessed: Mar. 29, 2025. [Online]. Available: https://www.fia.com/system/files/documents/fia_2025_formula_1_sporting_regulations_-_issue_4_-_2025-02-26.pdf

[33] M. Nakagawa, S. Kallweit, F. Michaux, and T. Hojo, 'Typical Velocity Fields and Vortical Structures around a Formula One Car, based on Experimental Investigations using Particle Image Velocimetry', *SAE International Journal of Passenger Cars - Mechanical Systems*, vol. 9, no. 2, pp. 2016-01–1611, Apr. 2016, doi: 10.4271/2016-01-1611.

[34] Mustafa Cavcar, 'The International Standard Atmosphere (ISA)', *Anadolu University, Turkey*, vol. 30, no. 9, pp. 1–6, 2000.

[35] N. Tom Benson, 'Wing Geometry Definitions', Glenn Research Centre. Accessed: Mar. 15, 2025. [Online]. Available: https://www.grc.nasa.gov/www/k-12/VirtualAero/BottleRocket/airplane/geom.html#top

Appendices

Appendix A: Tab and Plate Drawings

(Drawings provided in supplementary CAD files as per submission instructions)

All inserts (x6) identical

DETAIL A
SCALE 2 : 1

DRAWN		
mseest	02/02/2025	max.stancliffe.2021@uni.strath.ac.uk
CHECKED		07961651760
QA		TITLE
MFG		Plate – 1 Required
APPROVED		

SIZE **D** · DWG NO **Plate** · REV

SCALE 1 : 1 · SHEET 1 OF 1